J. Fluid Mech. (2000), *vol.* 423, *pp.* 175–203. Printed in the United Kingdom

Large-eddy simulation of a three-dimensional shear-driven turbulent boundary layer

By CHANDRASEKHAR KANNEPALLI AND UGO PIOMELLI

Department of Mechanical Engineering, University of Maryland, College Park, Maryland 20742, USA

(Received 8 October 1999 and in revised form 26 May 2000)

A three-dimensional shear-driven turbulent boundary layer over a flat plate generated by moving a section of the wall in the transverse direction is studied using large-eddy simulations. The configuration is analogous to shear-driven boundary layer experiments on spinning cylinders, except for the absence of curvature effects. The data presented include the time-averaged mean flow, the Reynolds stresses and their budgets, and instantaneous flow visualizations. The near-wall behaviour of the flow, which was not accessible to previous experimental studies, is investigated in detail. The transverse mean velocity profile develops like a Stokes layer, only weakly coupled to the streamwise flow, and is self-similar when scaled with the transverse wall velocity, W_s. The axial skin friction and the turbulent kinetic energy, K, are significantly reduced after the imposition of the transverse shear, due to the disruption of the streaky structures and of the outer-layer vortical structures. The turbulent kinetic energy budget reveals that the decrease in production is responsible for the reduction of K. The flow then adjusts to the perturbation, reaching a quasi-equilibrium three-dimensional collateral state. Following the cessation of the transverse motion, similar phenomena take place again. The flow eventually relaxes back to a two-dimensional equilibrium boundary layer.

1. Introduction

Many engineering flows, such as those on swept wings of aircraft, rotating hubs of propellers, missiles, and rotating disks, at junctions of rotating and stationary walls of fluid machinery, and inside curved ducts or bends etc. are three-dimensional in nature. Thus, a study of three-dimensional turbulent boundary layers (TBLs) is of great practical relevance. Three-dimensional TBLs can be classified (Bradshaw 1987) as being either 'skew-induced' (Prandtl's first kind of secondary flow), if the three-dimensionality is introduced by a moving surface ('shear-driven') or by a cross-stream pressure gradient ('pressure-driven'), or 'stress-induced' (Prandtl's second kind of secondary flow). Reviews of recent work on 3DTBLs can be found in Johnston (1970), Fernholz & Vagt (1981), Cousteix (1986), Bradshaw (1987), Sendstad & Moin (1992), and Johnston & Flack (1996).

This investigation concentrates on the study of a three-dimensional shear-driven TBL. In nature, shear-driven flows occur on rotating hubs of propellers, missiles, and rotating disks, and at junctions of rotating and stationary walls in fluid machinery. Unlike pressure-driven 3DTBLs generated by the presence of an obstacle, no streamwise pressure-gradient is present in shear-driven TBLs; thus, the effects of

three-dimensionality can be completely separated from those of acceleration. 3DTBLs free of adverse pressure gradients can be generated by introducing mean streamwise vorticity at the wall (i.e. by applying an impulsive spanwise motion to the wall). In the absence of additional sources of three-dimensionality, all three-dimensional effects grow outwards from the wall.

Several experimental investigations of shear-driven boundary layers of this type have been carried out. In most of them the geometry is a cylinder with a spinning section. The measurements can be carried out either on the spinning part, to study the response of the boundary layer to the imposition of the three-dimensionality, or else downstream of it, to investigate the return to equilibrium of the boundary layer. Bissonnette & Mellor (1974) studied the flow over the spinning section, and found that the flow was collateral (i.e. the direction of the mean velocity remained the same at each y) near the wall, while away from the wall the flow became three-dimensional. The streamwise wall stress increased slightly over the spinning section of the cylinder, while the spanwise wall stress increased over the moving part, and decreased on the stationary part. They found that the Reynolds-stress angle lagged behind the mean-velocity-gradient angle and that the eddy viscosity in the spanwise direction was significantly smaller than the streamwise one, an effect that they argued was at least in part due to the curvature. This result suggests that eddy-viscosity models for the Reynolds-averaged Navier–Stokes equations may have difficulties in this type of flow. Following Clauser (1954), they used a coordinate system that moved with the wall in the spanwise direction and was aligned with the free-stream relative velocity ($U_\infty^2+W_s^2$) (where W_s is the wall velocity and U_∞ the free-stream velocity), and found that the slope of the logarithmic law was considerably lower than in two-dimensional flows.

Lohmann (1976) used larger surface-to-free-stream velocity ratios in his spinning-cylinder experiments. He found that the transverse velocity boundary layer grew at a rate approximately proportional to $x^{1/2}$, where x was measured from the beginning of the moving section. In the region close to the wall, the transverse mean velocity distribution and wall-stress component attained an asymptotic state in an axial distance of about ten initial boundary layer thicknesses. The Reynolds stresses were substantially increased, which led to significant differences in the streamwise mean velocity profiles: a velocity deficit developed that propagated outwards. The layer was collateral throughout the moving region. For the lower wall velocity, $W_s/U_\infty = 1.45$, the axial wall stress first increased, then decreased slightly and finally continued to increase toward a new steady state; at the higher wall speed, $W_s/U_\infty = 2.2$, on the other hand, no decrease was observed, although the wall stress had a constant region downstream of the leading edge of the moving section. The energy in the large-scale structures initially decreased, suggesting that the three-dimensionality also has an effect on the distribution of scales in the wall region. As in the experiment of Bissonnette & Mellor (1974), the stress angle was found to lag the mean-velocity-gradient angle.

A further experimental and computational study was performed by Higuchi & Rubesin (1979). They studied the cross-flow on the stationary section of the cylinder immediately downstream of a spinning section. Their computations showed that models that accounted for the anisotropy of the eddy viscosity predicted the cross-flow better than those that used a scalar eddy viscosity.

Continuing the work of Higuchi & Rubesin (1979), Driver & Hebbar (1987) measured velocity and Reynolds stresses in the boundary layer on a cylinder with a rotating section using laser-Doppler velocimetry (LDV). Measurements were taken primarily on the stationary section where the flow was relaxing from a three-

dimensional boundary layer back to a two-dimensional state. In agreement with the previous investigations, they found that in this recovery region the eddy viscosity became anisotropic, especially in the inner region, where the stress lags the mean velocity gradient. They also found a local minimum of the Reynolds shear stress $\langle u'v' \rangle$ near the wall ($\langle \cdot \rangle$ denotes an ensemble average and a prime the velocity fluctuations), whereas the structure parameter $a_1 = (\langle u'v' \rangle^2 + \langle v'w' \rangle^2)^{1/2} / \langle u_i' u_i' \rangle$ increased slightly at the beginning of the recovery region. Their measurements were concentrated in the recovery region, where the flow returns to a two-dimensional, equilibrium state, and their first measurement point was at $y^+ = 40$, where most of the flow turning has already occurred. More complete measurements using the same experimental setup were later collected by Driver & Johnston (1990).

A related flow was studied by direct simulation (DNS) of the Navier–Stokes equations by Moin *et al.* (1990). Starting from a fully developed two-dimensional plane channel flow, they suddenly imposed a spanwise pressure gradient. A transverse boundary layer developed at the wall, and propagated outwards. They observed a pronounced reduction of the turbulent kinetic energy following the imposition of the transverse pressure gradient. This decrease was attributed to a decrease in the production of turbulent kinetic energy, which was, in turn, caused by suppression of the pressure–strain mechanism for inter-component energy transfer: the decrease of this term caused a suppression of the wall-normal Reynolds stress $\langle v'^2 \rangle$, and a decrease in the production of the shear stress $\langle u'v' \rangle$. Durbin (1993), however, pointed out that a reduced redistribution would also probably result in an increase of the streamwise Reynolds stress $\langle u'^2 \rangle$, which is contrary to the observations. The structure parameter, a_1, was found to decrease as the transverse pressure gradient was applied. They also observed the lag between the Reynolds shear stress angle and the mean velocity gradient angle.

Later, Sendstad & Moin (1992) used this database (as well as additional calculations in similar configurations) to study the response of the turbulent eddies to the three-dimensionality. They found that the reduction of the Reynolds shear stress $\langle u'v' \rangle$ is due to a weakening of the ejection and sweep events. They also observed a breakup of the turbulent streaks during the initial period.

Coleman, Kim & Le (1996) performed direct numerical simulations (DNS) of shear-driven channel flows. The flow was obtained by an impulsive spanwise motion of the lower wall of a plane channel in fully developed turbulent flow. A transverse boundary layer developed in time. Their conclusions are consistent with the experimental and numerical findings related above. They also observed an initial decrease of the streamwise wall stress, which later recovers. The turbulent kinetic energy also decreased initially. They claimed that the most significant (but not the only) effect of shear-driven three-dimensionality is a modification of the near-wall streaks and/or of the interaction between the streaks and quasi-streamwise vortices, rather than a direct modification of the vortices.

These studies have revealed a few salient features of such flows: the shear-stress angle lags the strain angle, the eddy viscosity is anisotropic, the turbulent kinetic energy and the streamwise wall shear initially decrease as a consequence of structural changes in the coherent eddies in the wall layer; the structure parameter a_1 decreases. Simple low-level models based on an isotropic eddy viscosity, which forces the Reynolds-stress angle to be in phase with the velocity-gradient angle, cannot in general be assumed to be valid for this flow. Indeed when such models were applied to three-dimensional shear-driven or pressure-driven flows, they yielded poor results (Fannelop & Krogstad 1975; Bradshaw, Launder & Lumley 1996). Ölçmen & Simpson

(1993) reviewed the performance of four different algebraic eddy-viscosity models and concluded that no model could perform well in all the cases studied. In general, models that accounted for the anisotropy of the eddy viscosity (Rotta 1979) performed better; even in those cases, however, the anisotropic constants needed adjustment for different flows. Some of the features of 3DTBLs, such as the reduction in the Reynolds shear stress, were not captured at all by any of these models.

A Reynolds stress model with a modification to the ϵ equation (Durbin 1993) was shown to reproduce some of the features observed by Moin *et al.* (1990) in a three-dimensional turbulent channel flow, most importantly the drop in the turbulent kinetic energy. Based on his results, Durbin (1993) concludes that the primary cause of the three-dimensional effect may be the increase in the rate of energy dissipation (ϵ), which causes the decrease in the turbulent kinetic energy. Indeed, Moin *et al.* (1990) saw an increase of ϵ around $y^+ \simeq 10$, although this was accompanied by a reduction close to the wall. Parneix & Durbin (1997) also obtained good results in simulations of three-dimensional boundary layers using the *V2F* model.

Despite the progress brought about by the experimental and numerical studies, there are still several unanswered questions. Given their cost, DNS to date have been limited to temporal evolutions, and to the early stages of the development only: Moin *et al.* (1990) did not examine at all the recovery of the flow after the initial decrease, and Coleman *et al.* (1996), whose calculations extend to times in which the turbulent kinetic energy and wall shear have recovered the two-dimensional value, also concentrate on the initial stages. Spatially developing flows, moreover, have only been studied experimentally, and the measurements do not provide sufficient information on the physics of 3DTBLs in the near-wall region (where most of the flow turning occurs) that is required to develop improved models for engineering design and analysis.

Large-eddy simulations (LES) can play a useful role in bridging the gap between the detailed information on the early development of the 3DBL obtained from DNS, and the more global, but less detailed knowledge gained from the experiments. LES have been applied with some success, recently, to three-dimensional flows (Liu, Piomelli & Spalart 1996; Wu & Squires 1998; Huai, Joslin & Piomelli 1999), and it has been shown that they are capable of predicting them with sufficient accuracy, and at a smaller cost than DNS.

In the present research, LES calculations are carried out for a three-dimensional shear-driven boundary layer over a flat plate. The configuration is similar to the spinning cylinder studied experimentally (Bissonnette & Mellor 1974; Lohmann 1976; Driver & Hebbar 1987; Driver & Johnson 1990); curvature effects are, however, absent. Unlike pressure-driven three-dimensional flows, in which it is difficult to separate the effects of three-dimensionality from those of pressure gradients, a shear-driven boundary layer isolates the effect of three-dimensionality due to the wall shear. In this flow all effects of three-dimensionality will grow outward from the wall, unlike some pressure-driven flows in which inviscid skewing and streamwise pressure gradients may affect the turbulence. Hence this work is a study of three-dimensionality in the near-wall turbulence. The use of LES allows a detailed investigation to be performed, using the Reynolds stress budgets in conjunction with flow visualization, on the mechanisms that alter the structure of the turbulence, and in particular the Reynolds stresses and the skin friction, in such flows. Despite the reduced cost of LES compared to DNS, however, this simulation was still fairly expensive, due to the build-up of small-scale energy-carrying eddies in the three-dimensional region of the flow that needed to be resolved. For this reason, the Reynolds numbers of the

experimental investigations could not be matched, and an extensive parametric study could not be performed. This brought about some difficulty in comparing the LES results with experimental data, as will be shown later. The problem formulation and the numerical method are described in the next Section, followed by a description of the problem configuration and the simulation parameters. The results will then be presented, and some conclusions will be drawn.

2. Problem formulation

In large-eddy simulations, the flow variables are decomposed into a large-scale (or resolved) component, and a subgrid-scale (or unresolved) one through the filtering operation; a filtered variable is defined as

$$\overline{f}(\boldsymbol{x}) = \int_D f(\boldsymbol{x}')G(\boldsymbol{x}, \boldsymbol{x}')\,\mathrm{d}\boldsymbol{x}', \tag{2.1}$$

where $G(\boldsymbol{x})$ is the filter function and D is the computational domain. Applying the filtering operation to the incompressible Navier–Stokes and continuity equations yields the governing equations of motion for the large-scale velocity,

$$\frac{\partial \overline{u}_i}{\partial t} + \frac{\partial \overline{u}_i \overline{u}_j}{\partial x_j} = -\frac{\partial \overline{p}}{\partial x_i} - \frac{\partial \tau_{ij}}{\partial x_j} + \frac{1}{Re_r}\frac{\partial^2 \overline{u}_i}{\partial x_j \partial x_j}, \tag{2.2}$$

$$\frac{\partial \overline{u}_i}{\partial x_i} = 0. \tag{2.3}$$

Here $\overline{p} = \overline{P}/\rho$, P is the pressure and ρ the density of the fluid, and $\overline{u}_i$ is the filtered velocity; x_1 or x, x_2 or y and x_3 or z represent the streamwise, wall-normal and spanwise directions, respectively, while t represents the time. The velocities u_1, u_2, and u_3 in the x-, y-, and z-directions are used interchangeably with u, v, and w. Equations (2.2)–(2.3) are non-dimensionalized by the free-stream velocity, U_∞, and a reference length δ_r^*; the reference Reynolds number is thus defined as $Re_r = U_\infty \delta_r^*/\nu$, where ν is the kinematic viscosity of the fluid.

The coupling between the large and the small scales appears in the form of a subgrid-scale stress tensor $\tau_{ij} = \overline{u_i u_j} - \overline{u}_i \overline{u}_j$ that needs to be modelled. Since the small scales tend to be more universal than the large ones, their effects are commonly modelled by simple eddy-viscosity models of the form

$$\tau_{ij} - \delta_{ij}\,\tau_{kk}/3 = -2\nu_T \overline{S}_{ij} = -2\,C\overline{\Delta}^2 |\overline{S}|\,\overline{S}_{ij}, \tag{2.4}$$

where ν_T is the eddy viscosity, δ_{ij} is the Kronecker delta, $\overline{S}_{ij} = (\partial \overline{u}_i/\partial x_j + \partial \overline{u}_j/\partial x_i)/2$ is the large-scale strain-rate tensor, $|\overline{S}| = (2\overline{S}_{ij}\overline{S}_{ij})^{1/2}$, and $\overline{\Delta} = 2(\Delta x \Delta y \Delta z)^{1/3}$ is the filter width. C is a dimensionless model coefficient that, in this work, is evaluated by the localized version (Piomelli & Liu 1995) of the dynamic eddy-viscosity model (Germano *et al.* 1991; Lilly 1992). The test filter is a top-hat filter in real space, applied by a three-point averaging using the trapezoidal rule. The total viscosity, $\nu + \nu_T$, is constrained to be non-negative to ensure numerical stability of the time integration. In addition, the numerator and denominator of the model coefficient are smoothed over the test-filter width by using local three-point averaging in space (Zang, Street & Koseff 1993; Piomelli & Liu 1995). This model has been used successfully for the prediction of three-dimensional transitional and turbulent flows (Liu *et al.* 1996; Huai, Joslin & Piomelli 1997, 1999) similar to the one under investigation.

The governing equations (2.2)–(2.3) are solved using a fractional-step method

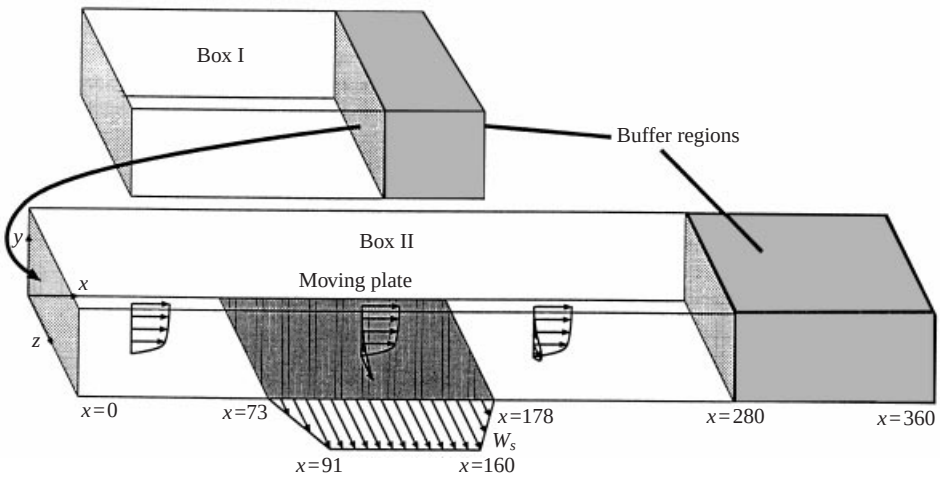

FIGURE 1. Problem setup.

(Chorin 1967). For the momentum equation, fourth-order central differences are used in the streamwise direction, x, Chebychev series in the wall-normal one, y, and Fourier series in the spanwise direction, z. The time-advancement is performed by an implicit Crank–Nicolson scheme for the wall-normal diffusion; all the other terms are advanced explicitly using a compact third-order Runge–Kutta method. The Poisson equation for the pressure is discretized in a similar manner (compact fourth-order differences are used in x, however) and solved by an influence matrix method. The numerical method was validated by Joslin, Streett & Chang (1993) and Huai *et al.* (1997, 1999).

No-slip conditions are applied at the solid surface; periodicity is imposed in the span-wise direction, and the perturbations are required to vanish in the free stream. At the outflow, the buffer-domain technique (Streett & Macaraeg 1989) is used, in which the governing equations are gradually parabolized in a buffer region appended to the computational domain.

In the present study a three-dimensional shear-driven flow is investigated, in which the three-dimensionality is introduced by surface shear. A two-dimensional equilibrium boundary layer over a flat plate is subjected to a sudden perturbation imposed by the sideways motion of a section of the wall, as illustrated in figure 1. After the moving section of the wall, the boundary layer is allowed to return towards an equilibrium two-dimensional state on another stationary section.

To simulate a spatially developing turbulent boundary layer, one must use a computational domain that is long enough in the streamwise direction that the flow passes through a region of laminar growth, undergoes laminar breakdown/transition and finally reaches the turbulent state desired. To accomplish the whole process in one simulation (i.e. in one computational domain) requires a very long box and, consequently, a large number of grid points, thus making the calculation very expensive. A possible alternative is to break up the computational box into several sub-domains, and perform smaller simulations on each of these sub-domains successively. In the present simulation two computational boxes were used (see figure 1). In the first one the flow is initially laminar and begins transition to turbulence. Incidentally, the reference length δ_r^* is the displacement thickness at the inflow of the first box. The flow field in a plane at a chosen streamwise location after the flow transitions is

	NS	LS	HSC	HSM	HSF
L_x	360	360	360	360	360
L_y	100	100	100	100	100
L_z	25	25	25	25	25
W_s/U_∞	0.0	0.3	1.0	1.0	1.0
N_x	561	561	561	1121	1121
N_y	65	65	65	65	65
N_z	33	33	33	33	65
Δx	0.64	0.64	0.64	0.32	0.32
Δy_{min}	0.006	0.006	0.006	0.006	0.006
Δz	0.79	0.79	0.79	0.79	0.39
Δx^+	21.0	22.0	23.0	12.0	12.0
Δy^+_{min}	0.19	0.20	0.22	0.23	0.23
Δz^+	26.0	27.0	29.0	30.0	15.0

TABLE 1. Configuration and grid parameters for the shear-driven boundary layer simulations.

saved over a sufficiently long period of time as the outflow data from this box. This time sequence of data is used as the inflow for the simulation in box II, which is fully turbulent. This technique has been used successfully by Huai *et al.* (1997, 1999). The inflow data for Box I is taken from the simulations of Huai *et al.* (1997).

The domain of the 3DBL simulation is shown in figure 1. The spanwise motion of the wall is imposed between the streamwise locations $x/\delta_r^* = 73$ and $x/\delta_r^* = 178$. Unlike in the experiments, in which the transverse velocity was discontinuous at the edges of the spinning section, in the computations the transverse wall velocity had to be transitioned smoothly over a distance $18\delta_r^*$ to ensure numerical stability. The code uses fourth-order-accurate differencing schemes in the streamwise direction, which generate oscillations when a sharp interface is encountered. Several smoothing distances were tried, and values lower than the one eventually used resulted either in explosive instability of the code, or else required very small time steps, that would have made the calculation unfeasible. Two different values of the spanwise wall-to-free-stream velocity ratio $W_s/U_\infty = 0.3$ and 1.0 are used, referred to as 'low shear' (LS) and 'high shear' (HS) cases. A simulation with no shear was also carried out, and will be referred to as the 'no shear' (NS) case. Three simulations with $W_s/U_\infty = 1.0$ were carried out, with a coarse, medium and fine mesh; they are referred to as HSC, HSM and HSF cases, respectively. A summary of the simulation and configuration parameters can be found in table 1. In this table, the grid sizes in wall variables are based on the time- and plane-averaged friction velocity $Q_\tau = (\tau_{w,x}^2 + \tau_{w,z}^2)^{1/4}$, where $\tau_{w,x} = \mu[\partial U/\partial y]_w$, $\tau_{w,z} = \mu[\partial W/\partial y]_w$, and a capital letter denotes a time-averaged quantity.

Grid points are evenly distributed in the streamwise (x) and spanwise (z) directions. In the wall-normal direction, the grid points are clustered in the near-wall region. A buffer region with a streamwise extent of $79\delta_r^*$ is appended at the end of each computational box for the numerical treatment of the outflow.

3. Results

3.1. *Simulation validation*

Figure 2, which shows the spanwise velocity contours for the HSM case, can be used to illustrate the general features of the flow field prior to a quantitative validation of the

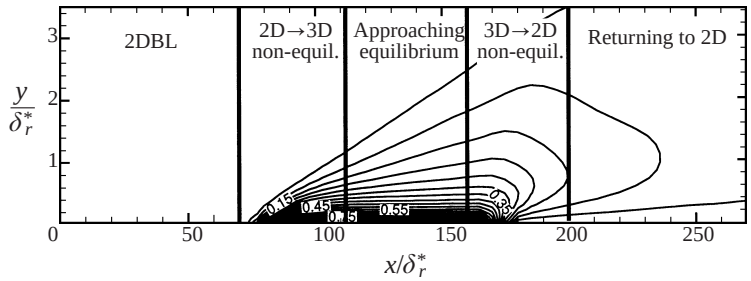

FIGURE 2. Contours of W: 20 equi-spaced contours are shown between 0.05 and 1. $W_s/U_\infty = 1$, intermediate grid (HSM).

simulations and analysis of the data. Five regions of the flow can be identified. Downstream of a two-dimensional turbulent boundary layer is a highly non-equilibrium region following the imposition of the spanwise velocity at the wall. Subsequently, the flow begins to re-equilibrate and approaches a collateral state. At the trailing edge of the plate, however, a new perturbation is applied that again moves the flow away from equilibrium. The two-dimensional equilibrium state is finally approached again. The gradual increase of the wall velocity at the leading edge, and decrease at the trailing edge, are also evident in the figure.

The validation of the present simulations consisted of two stages. First, a resolution study was carried out to determine that grid-converged results had been achieved; then, the LES results were compared with experimental data. The grid resolution study was performed in the high-shear case. As mentioned above, three meshes were used, coarse, medium and fine. The respective resolutions are reported in table 1. The equations of motion were integrated for $820\delta_r^*/U_\infty$; the first- and second-order statistics obtained by averaging over only half of the sample differed from those obtained using the full sample by less than 2%. The Reynolds-stress budgets, on the other hand, were averaged over a shorter period, $205\delta_r^*/U_\infty$. The convergence of the Reynolds-stress statistics is less satisfactory: using only half of the sample gave statistics that differed from those obtained from the full sample by 5–10%. All the trends that will be discussed later, however, are independent of the sample size.

Mean velocity profiles at four representative locations in the regions described above are shown in figure 3. The inset shows their location with respect to the contours shown in figure 2. The velocity and distance from the wall are normalized using the kinematic viscosity ν and the local (time-averaged) friction velocity Q_τ defined above. In the two-dimensional regions before and after the moving plate the coarse grid is sufficient to capture the turbulent eddies. The results obtained on all grids, therefore, collapse. In the three-dimensional and in non-equilibrium regions, on the other hand, smaller scales are generated, and finer grids are required to resolve the sharp gradients present in the flow. The medium- and fine-mesh results, therefore, diverge from the coarse-grid ones. They are, however, in good agreement with each other, indicating that the medium mesh, which has twice the streamwise resolution of the coarse one, is sufficient to capture the essential phenomena of the flow. Spanwise refinement of the grid results in marginal improvements only. This is due to the fact that, in the non-equilibrium region, the flow turns very rapidly in the spanwise direction, forming an angle approaching 50° to the x-axis. The streamwise streaks are thus re-oriented in the spanwise direction, and the streamwise grid size must be small enough to capture these structures accurately. The profiles of the trace of the resolved

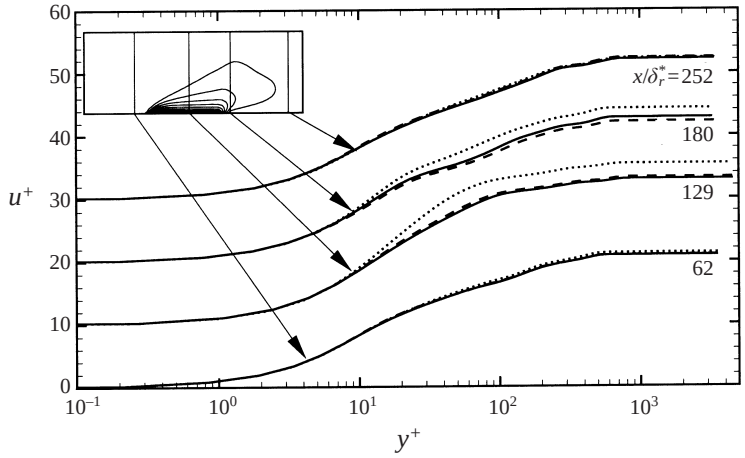

FIGURE 3. Mean velocity profiles for different grid resolutions. $W_s/U_\infty = 1.0$. ·····, Coarse; ———, medium; – – – –, fine.

Reynolds stress tensor $q^2 = \langle u_i' u_i' \rangle$ (here and in the following the angle brackets denote time averaging, and a prime the resolved part of the fluctuating quantities, defined as $f' = \overline{f} - \langle f \rangle = \overline{f} - F$) exhibit the same trends.

Two sets of experiment are relatively close to the present configuration, and supply sufficient data for evaluation of the LES results: those by Lohmann (1976), which will be henceforth referred to as L76, and the related ones by Driver & Hebbar (1987) and Driver & Johnston (1990), which will be referred to as DH87 and DJ90. The direct comparison of the LES results with the experimental data is made difficult by several differences between the experimental and numerical configurations. First, the experiments were carried out in cylindrical configurations, whereas the LES used a flat-plate geometry. Since in the experiments the boundary-layer thickness is fairly small compared to the cylinder diameter (less than 10% for L76, 18% for DH87 and DJ90), this difference might not affect the results very significantly (see Neves, Moin & Moser (1994*a*, *b*) for a discussion of the effects of curvature on the boundary layer statistics). More significant is the Reynolds number difference. The experiments are respectively at $Re_\theta = 2420$ (L76) and 6000 (DH87 and DJ90). The present calculations are at $Re_\theta \approx 1100$. Higher values could not be reached due to the cost of the calculations: the medium-grid HSM case had nearly 2.5 million points, and required over 100 Cray C-90 CPU hours to obtain converged statistics. Matching the Reynolds number of L76 would have increased the cost of the calculation by over a factor of 10, over 150 times for DH87 and DJ90. An additional and also significant difference is created by the smooth transition, in the calculations, between the moving and stationary sections of the plate, which results in a more gradual development of the three-dimensional region after the leading and trailing edges of the plate, and also in some difficulty in comparing streamwise locations between LES and experiments. Finally, the L76 experiment had significantly higher wall velocities ($W_s/U_\infty = 1.45, 2.25$) and a longer moving section than any of the present calculations.

Despite these difficulties, some confidence in the LES results can be established. First, in figure 4, the mean velocity and q^2 in the two-dimensional region are compared with the DNS data of Spalart (1988). The agreement is quite good for both quantities. The present calculations, it should be remarked, are well-resolved LES, especially in the two-dimensional regions of the flow, and SGS modelling errors are not expected

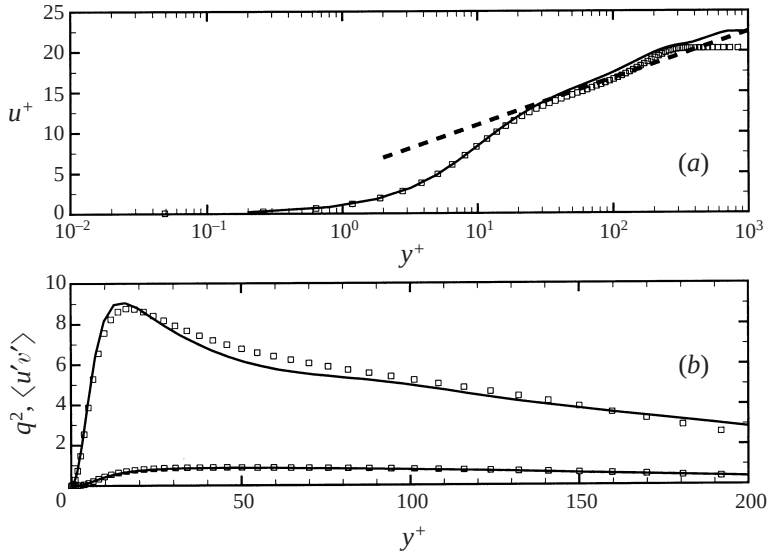

FIGURE 4. (*a*) Mean velocity profile and (*b*) trace of the Reynolds stress tensor in the two-dimensional region. ———, LES, $Re_{\delta^*} = 1740$; ○, DNS, $Re_{\delta^*} = 2000$ (Spalart 1988); ▬ ▬, $2.5 \log y^+ + 5.2$.

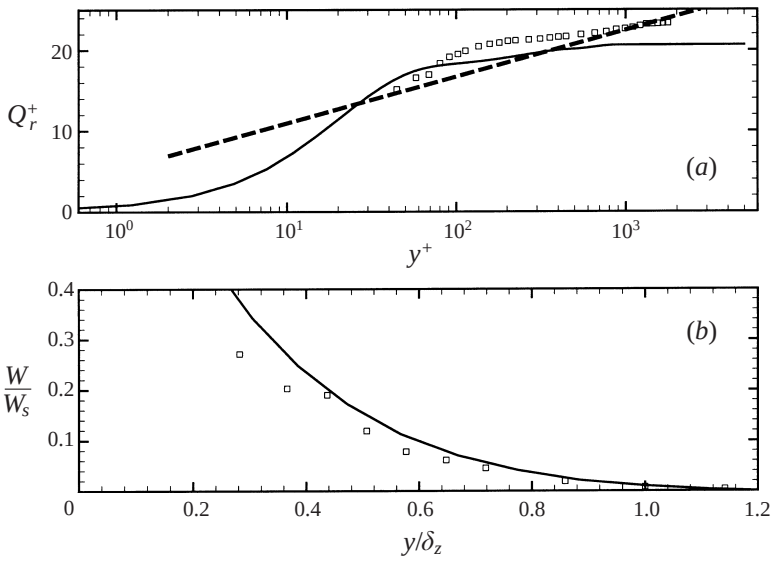

FIGURE 5. Mean velocity profiles on the moving plate. ———, LES, $x/\delta_r^* = 103$, $(x - x_{LE})/\delta_o = 1.4$; □, experiment, L76, $(x - x_{LE})/\delta_o = 1.25$; ▬ ▬, $2.5 \log y^+ + 5.2$.

to affect the results. The SGS shear stress τ_{12}, for instance is less than 2% of the resolved Reynolds stress on average, and never exceed 11% of $\langle u'v' \rangle$ over the entire flow field.

In figure 5 the velocity profiles on the moving plate are compared with the experimental data (L76). The velocity relative to the moving wall is defined as $\boldsymbol{Q}_r = U\boldsymbol{i} + (W - W_s)\boldsymbol{k}$ (where $\boldsymbol{i}$ and $\boldsymbol{k}$ are the unit vectors in the x- and z-directions). Q_r is normalized by the resultant friction velocity Q_τ, x_{LE} is the location of the leading edge of the moving plate (for the LES it was taken midway through the

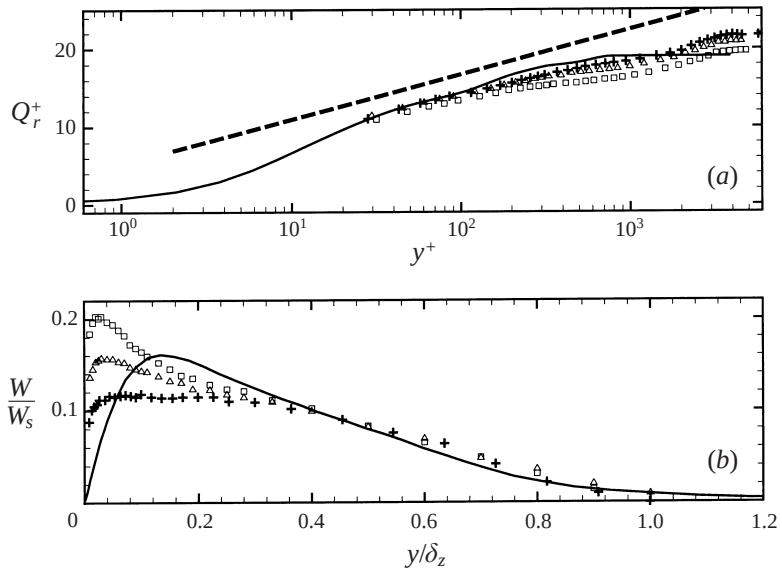

FIGURE 6. Mean velocity profiles in the recovery region. ———, LES, $x/\delta_r^* = 195$, $(x - x_{TE})/\delta_o = 1.8$; □, experiment, DJ90, $(x - x_{TE})/\delta_o = 0.9$; △, DJ90, $(x - x_{TE})/\delta_o = 1.8$; +, DJ90, $(x - x_{TE})/\delta_o = 3.6$; - - -, $2.5 \log y^+ + 5.2$.

smooth transition, at $x/\delta_r^* = 82$), and δ_o is the thickness of the boundary layer at x_{LE} in the absence of plate motion. Only qualitative agreement was obtained. The existence of a logarithmic layer with a lower slope than that corresponding to the von Kármán constant, however, can be observed in both the LES and the experiment. The slope predicted by the LES is also in good agreement with the experimental result. The spanwise velocity profile normalized by the wall velocity in outer coordinates (y is normalized by the thickness of the spanwise boundary layer, defined as the location where $W = 0.01 W_s$) agrees fairly well with the experimental data, given the uncertainty in determining the leading edge of the plate in the calculation, and the difference in Reynolds number and configuration (it will be shown later that the different wall velocity should not affect this comparison too significantly).

In figure 6 the resultant velocity Q_r and the mean spanwise velocity profiles in the recovery region are compared with the experimental measurements of DJ90. To circumvent the uncertain location of the trailing edge in the LES, three experimental profiles that bracket the LES location are shown. In the experiments, Q_r^+ was found to collapse on a logarithmic layer; the LES data follow this trend as well. The LES spanwise velocity profile agrees well with experiments in the outer layer. Near the wall, the differences are consistent with the Reynolds number difference, and with the smoother transition between the fixed and moving plates in the calculation.

Figure 7 shows the comparison of the skin-friction coefficients, $c_{f,x} = 2\tau_{w,x}/\rho U_\infty^2$ and $c_{f,z} = 2\tau_{w,z}/\rho U_\infty^2$, downstream of the moving plate between the simulation and the DJ90 experiment. Although a 30% difference is observed between the $c_{f,x}$ obtained from the simulations and the experimental data, this difference can be attributed to the large disparity in the Reynolds numbers, which in the experiment was six times higher than in the simulation. In 2DTBLs, $c_{f,x}$ can be approximated by

$$c_{f,x} \approx 0.02 Re_\delta^{-1/6} \tag{3.1}$$

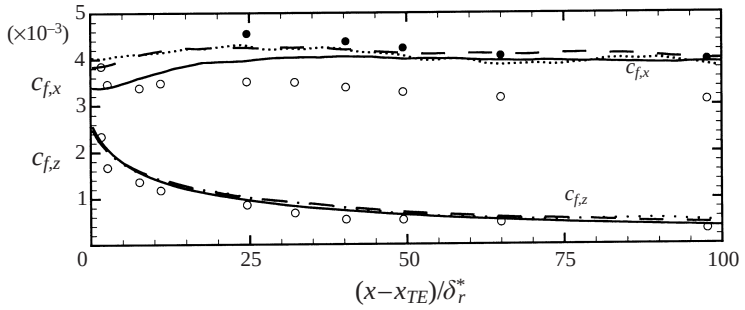

FIGURE 7. Streamwise variation of the skin-friction coefficients in the recovery region. $W_s/U_\infty = 1.0$. ·····, Coarse grid; ———, medium grid; – – – –, fine grid; ○, DJ90; ●, rescaled data from DJ90.

(White 1991). If the experimental $c_{f,x}$ is multiplied by $(Re_{\delta,exp}/Re_{\delta,LES})^{1/6}$ to reduce the Reynolds-number dependence of the results, in fact, the agreement is quite good. The figure also confirms that the medium and fine meshes give grid-converged results. The transverse skin-friction coefficient is in good agreement with the experiment, with no Reynolds-number correction. As will be shown later, the spanwise component of velocity behaves like an independent Stokes layer, decoupled from the streamwise direction. The similarity of the W/W_s profiles results in Reynolds-number independence of the spanwise component.

Although the experimental flow conditions were not matched exactly, so that a direct comparison between LES and experiments could not be carried out, we have tried in this section to validate the simulation results. It has been shown that the grid resolution is sufficiently fine that first and second moments are not affected by insufficient resolution. In the two-dimensional region the LES is in very good quantitative agreement with the reference DNS data. On the moving plate, the experiment by Lohmann (1976) and the LES have differences in configuration, Reynolds number and wall velocity; nonetheless, the qualitative changes observed in the experiment are also present in the LES data. In the recovery region, collapse of the resultant velocity onto the experimental data is observed, and agreement with the experimental skin-friction coefficient is achieved if a correction for the Reynolds-number difference is performed. Away from the wall, the spanwise velocity also agrees well with the experimental data; near the wall, differences may be due to the smooth transition between the moving section and the stationary one in the calculation, as well as to Reynolds number effects.

3.2. *Mean flow*

Figure 8 shows the streamwise variation of the skin-friction coefficients over the entire domain for the three cases. Sharp changes occur at the moving wall junctions. Immediately after the shear is applied $c_{f,x}$ exhibits a sharp drop that amounts to 11% for the LS case and 33% for the HS case. While these magnitudes depend on the function used to match the moving wall to the two-dimensional boundary layer, a similar drop in the wall stress was reported by Coleman *et al.* (1996) in the DNS of a shear-driven boundary layer in a channel. They observed a drop of 10% in the stress for a wall-to-centreline velocity ratio in the channel of 0.5. Also, they indicate that higher shear produces a larger wall-shear reduction. As the flow develops on the moving plate, $c_{f,x}$ starts increasing again; the spanwise motion of the wall supplies additional energy to the flow, whose Reynolds number increases. At the

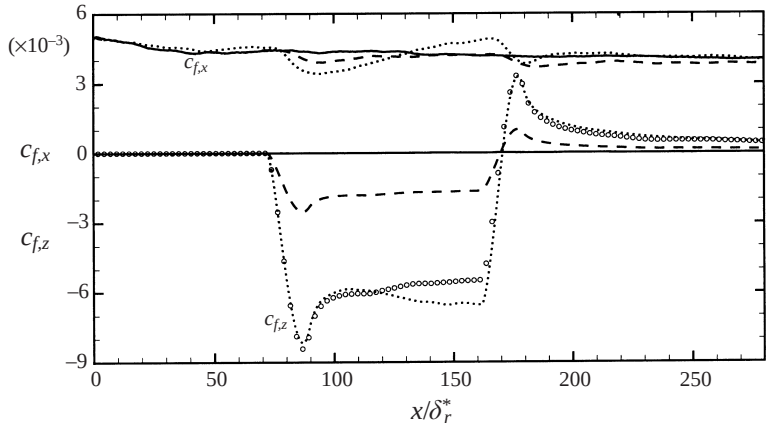

FIGURE 8. Streamwise variation of the skin-friction coefficients. ———, $W_s/U_\infty = 0$; – – – –, $W_s/U_\infty = 0.3$; ·····, $W_s/U_\infty = 1.0$; ○, $W_s/U_\infty = 0.3$, Lohmann's normalization.

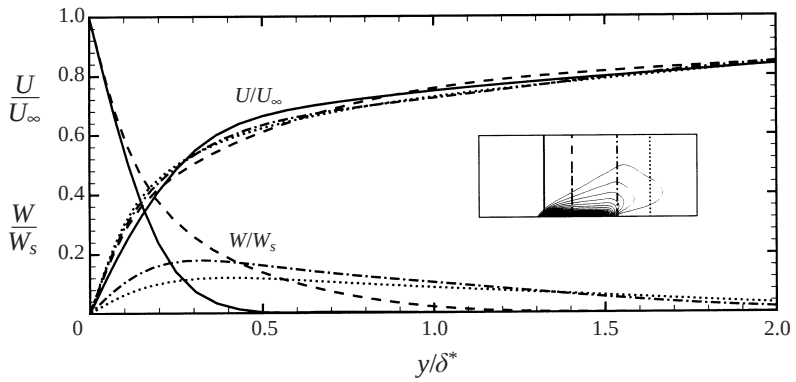

FIGURE 9. Mean velocity profiles for $W_s/U_\infty = 1.0$, HSM case. ———, $x/\delta_r^* = 93$; – – – –, $x/\delta_r^* = 129$; —·—, $x/\delta_r^* = 191$; ·····, $x/\delta_r^* = 216$.

trailing edge of the plate a new drop is observed, followed by a re-adjustment to the two-dimensional value.

The magnitude of the spanwise skin-friction coefficient, on the other hand, increases as soon as the shear at the wall is applied, goes through a short transient and then settles to a nearly constant value, an indication that a collateral state is approached. If, following L76, $\tau_{w,z}$ is made dimensionless by $\rho U_\infty W_s/2$ (for the HS case, this does not change its value, for the LS calculation this scaling is indicated by the circles in the figure) the profiles for both cases are much closer to each other, indicating that the transverse component may be self-similar with respect to the transverse wall velocity. This issue will be examined further later.

Figure 9 shows the mean U and W velocity profiles at several locations on the moving plate and in the recovery region for the HSM case. Lohmann (1976) observed a deficit in the axial mean velocity profile near the centre of the transverse boundary layer that moves outward as the transverse boundary layer grows. This effect is also observed in the present simulation, although not as pronounced as in the experiment, perhaps because of the lower transverse shear in the simulation. The effect is, in fact, more prominent for the higher shear case. Any significant change in U due to the

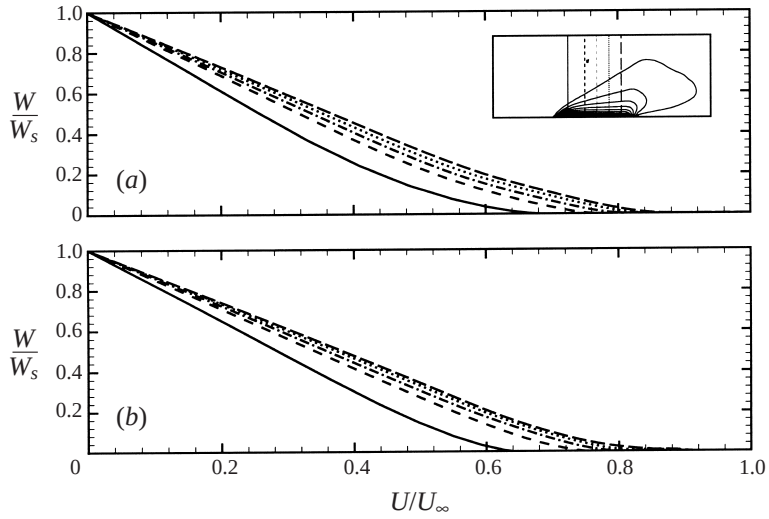

FIGURE 10. Polar velocity profiles. (*a*) LS; (*b*) HSM. ———, $x/\delta_r^* = 93$; – – – –, $x/\delta_r^* = 114$; —·—, $x/\delta_r^* = 129$; ·····, $x/\delta_r^* = 145$; — — —, $x/\delta_r^* = 160$.

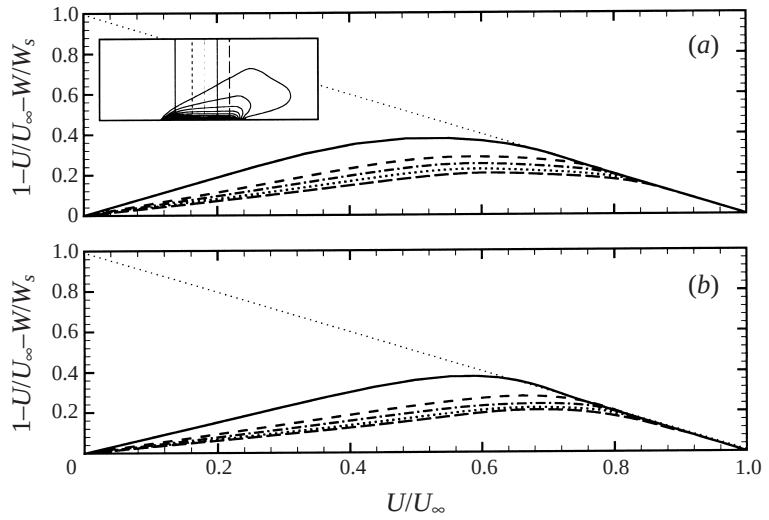

FIGURE 11. Polar velocity profiles. (*a*) LS; (*b*) HSM. ———, $x/\delta_r^* = 93$; – – – –, $x/\delta_r^* = 114$; —·—, $x/\delta_r^* = 129$; ·····, $x/\delta_r^* = 145$; — — —, $x/\delta_r^* = 160$.

imposition of spanwise shear can only occur indirectly due to changes in the Reynolds shear stress $\langle u'v' \rangle$. It can, therefore, be speculated that the structure of $\langle u'v' \rangle$ must be changed in this region. This issue will be further discussed in the next subsection.

The hodograph plots (Johnston 1960) of W/W_s and $1 - U/U_\infty - W/W_s$ vs. U/U_∞ are shown in figures 10 and 11 for the two shear cases. Notice that in figure 11 the straight dotted line corresponds to the two-dimensional state with $W = 0$, and the horizontal axis to the collateral condition ($U/U_\infty + W/W_s = 1$). Both figures reveal that the boundary layer at the end of the moving plate is moving towards the near-equilibrium collateral condition indicative of the flow having fully turned.

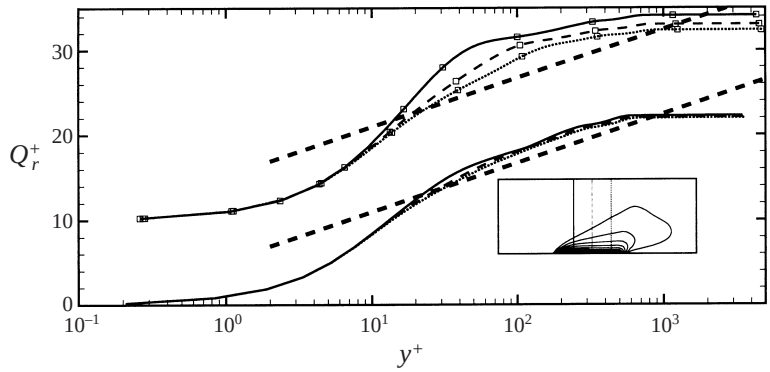

FIGURE 12. Relative velocity Q_r in wall variables. Lines: LS case; lines with symbols: HSM case. ———, $x/\delta_r^* = 103$; – – – –, $x/\delta_r^* = 128$; ·····, $x/\delta_r^* = 154$; ▬ ▬, $2.5 \log y^+ + 5.2$. The profiles for the HSM case are shifted upwards by 10 units for clarity.

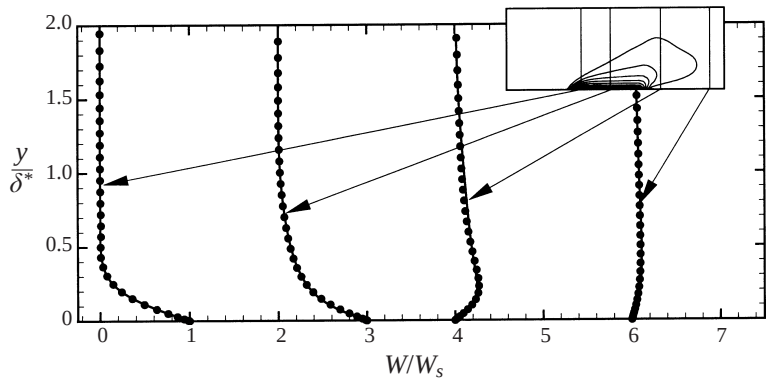

FIGURE 13. Mean spanwise velocity profiles. ———, $W_s/U_\infty = 1.0$, HSM case; ●, $W_s/U_\infty = 0.3$, LS case.

This condition has not, however, been reached in the present simulation, while both Driver & Hebbar (1987) and Lohmann (1976) achieved it in their experiments. Near the wall, where $W \simeq W_s$ and $U \simeq 0$, the relative velocity vector with respect to the wall velocity $W - s$ tends to the same slope as the calculated surface-flow angle, representing a region of nearly constant flow angle. The profiles for $x/\delta_r^* \geqslant 104$ have nearly the same slope near the wall, which implies that similarity on the moving wall may hold if expressed in terms of the velocity relative to the moving wall, $Q_r = \sqrt{U^2 + (W - W_s)^2}$ and the resultant friction velocity Q_τ defined previously.

The relative velocity Q_r is shown in figure 12 in semi-logarithmic coordinates. For the LS case, the velocity profiles collapse very well on a logarithmic region with the same slope as the two-dimensional boundary layer, albeit shifted slightly upwards. For the HS case, on the other hand, the logarithmic region has a lower slope, and no collapse is observed. The decrease of the slope of the logarithmic layer was also observed by Bissonnette & Mellor (1974) in their experiment, and by several researchers in other three-dimensional flows (Pierce & McAllister 1983*a*, *b*, *c*; Moin *et al.* 1990). The better collapse for the LS case is due to the fact that in this case the flow is closer to the collateral state, as also indicated by the constant value of the spanwise skin friction on the downstream part of the moving section.

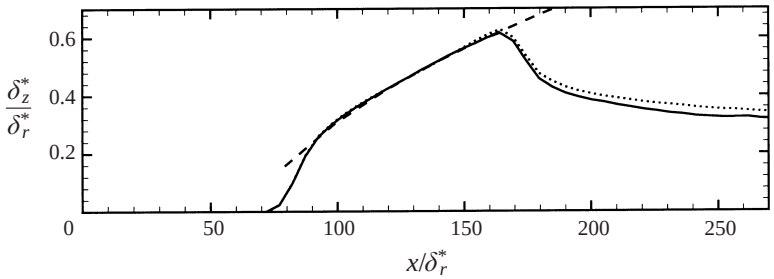

FIGURE 14. Displacement thickness of the transverse boundary layer. ———, $W_s/U_\infty = 0.3$; ·····, $W_s/U_\infty = 1.0$; – – –, $x^{1/2}$.

Figure 13 shows mean transverse-velocity profiles for the two shear cases. Near the wall, the velocity distribution progresses rapidly towards an asymptotic state, the shape of the profiles for $y/\delta^* < 0.5$ becoming essentially invariant towards the end of the moving plate, as also observed by L76. In the outer regions, the velocity distribution is far from an asymptotic state, as evidenced by the continuing growth of the transverse boundary layer and the change in shape of the velocity profile with downstream distance along the moving wall. Downstream of the moving plate, the mean W velocity close to the wall decays rapidly, while away from the wall, similar to the U velocity, it diffuses out very slowly. Comparison of the profiles at the two different surface speeds indicates that they are self-similar, and independent of the surface-to-free-stream velocity ratio. This indicates that the W velocity is decoupled from, or very weakly coupled to, the streamwise development.

This similarity of the spanwise velocity profiles is also evidenced in the transverse-boundary-layer displacement thickness, defined as

$$\delta_z^* = \int_0^\infty \frac{W(y)}{W_s}\,\mathrm{d}y, \tag{3.2}$$

and shown in figure 14. Near the upstream junction, where the flow first encounters the moving wall, δ_z^* undergoes a rapid growth; after a short adjustment distance, however, the growth rate settles to a power law proportional to $x^{1/2}$. Lohmann (1976) remarked that this growth rate is identical to the $\frac{1}{2}$ power at which Antonia & Luxton (1971) observed the influence of a smooth- to rough-wall boundary-condition change propagate into an existing boundary layer. The $x^{1/2}$ behaviour can also be associated with a diffusive process, similar to the $\delta \sim t^{1/2}$ behaviour observed for the laminar Stokes layer, for instance.

To clarify further this issue, the terms in the spanwise momentum equation were examined. Within the boundary-layer assumption, this equation reads

$$0 = -\left(\frac{\partial UW}{\partial x} + \frac{\partial VW}{\partial y}\right) + \nu\frac{\partial^2 W}{\partial y^2} - \frac{\partial\langle v'w'\rangle}{\partial y}. \tag{3.3}$$

Figure 15 shows the behaviour of these terms for the HSM case in the middle of the moving plate. The advection is dominated by the x-derivative; the viscous diffusion and $\langle v'w'\rangle$ Reynolds stress terms are particularly high at the junctions, but remain significant all along the moving plate. At the location shown, a subtle balance governs the momentum transport. Very near the wall ($y/\delta_r^* < 0.1$) advection and viscous diffusion are the only non-zero terms. Then, for $y/\delta_r^* < 0.5$, viscous diffusion and turbulent diffusion nearly balance, and the advection term is zero.

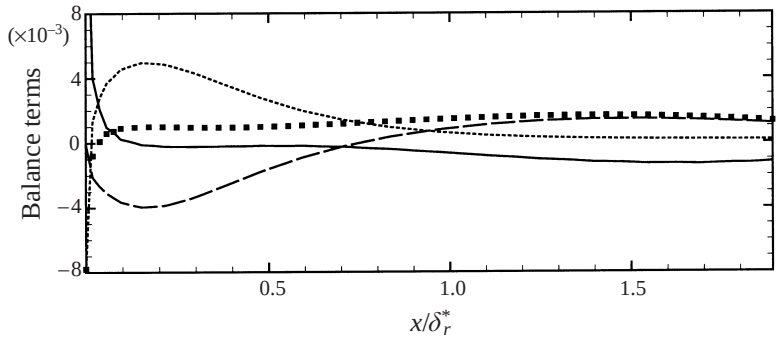

FIGURE 15. Terms in the time-averaged spanwise momentum balance equation; $x/\delta_r^* = 130$, $W_s/U_\infty = 1.0$. ———, Advection; ·····, viscous diffusion; – – – –, turbulent diffusion; ■, sum of viscous and turbulent diffusion.

Finally, in the outer region $y/\delta_r^* > 0.5$, advection gives a significant contribution, and balances the total diffusion, the sum of turbulent and viscous. Throughout most of the layer the advection term is nearly constant, and balances a combination of viscous and turbulent diffusion; the diffusion mechanism that causes the $x^{1/2}$ growth of the displacement thickness, therefore, appears to be due to an effective viscosity $\nu + \nu_{E,z}$, where $\nu_{E,z} = -\langle v'w' \rangle / (\partial W / \partial y)$. The important role of the turbulent diffusion may partly explain the agreement of the spanwise skin friction with the experimental data, independent of the Reynolds number difference.

3.3. *Second moments*

To understand better the phenomena that occur in the shear-driven boundary layer, consider the transport equation for the large-scale Reynolds stresses $\mathscr{R}_{ij} = \langle u_i' u_j' \rangle$:

$$\frac{\partial \mathscr{R}_{ij}}{\partial t} + U_k \frac{\partial \mathscr{R}_{ij}}{\partial x_k} = \mathscr{P}_{ij} - \mathscr{E}_{ij} + \mathscr{D}_{ij} + \Pi_{ij} \tag{3.4}$$

where

$$\mathscr{P}_{ij} = -\left(\mathscr{R}_{ik} \frac{\partial U_j}{\partial x_k} + \mathscr{R}_{jk} \frac{\partial U_i}{\partial x_k} \right), \tag{3.5}$$

$$\mathscr{E}_{ij} = 2\nu \left\langle \frac{\partial u_i'}{\partial x_k} \frac{\partial u_j'}{\partial x_k} \right\rangle - \left\langle \tau_{ik} \frac{\partial u_j'}{\partial x_k} + \tau_{jk} \frac{\partial u_i'}{\partial x_k} \right\rangle, \tag{3.6}$$

$$\mathscr{D}_{ij} = \frac{\partial}{\partial x_k} \left[\nu \frac{\partial \mathscr{R}_{ij}}{\partial x_k} - \langle u_i' u_j' u_k' \rangle + \langle \tau_{jk} u_i' + \tau_{ik} u_j' \rangle \right], \tag{3.7}$$

$$\Pi_{ij} = -\left\langle u_i' \frac{\partial p'}{\partial x_j} + u_j' \frac{\partial p'}{\partial x_i} \right\rangle, \tag{3.8}$$

are the production, dissipation, diffusion (viscous and turbulent) and velocity–pressure-gradient terms respectively (Speziale 1991). The dissipation and turbulent diffusion consist of two parts: a large-scale and an SGS contribution. The transport equation for the resolved turbulent kinetic energy, $K = \langle u_i' u_i' \rangle / 2$ can be obtained by contracting equation (3.4) for $i = j$ and multiplying by one half.

Profiles of the Reynolds stresses $\langle u_i' u_j' \rangle$ at several locations are shown in figure 16. In the two-dimensional region, the expected distribution is obtained: $\langle u'^2 \rangle$ is the most significant of the normal stresses, $\langle u'v' \rangle$ the only non-zero shear stress. As the wall

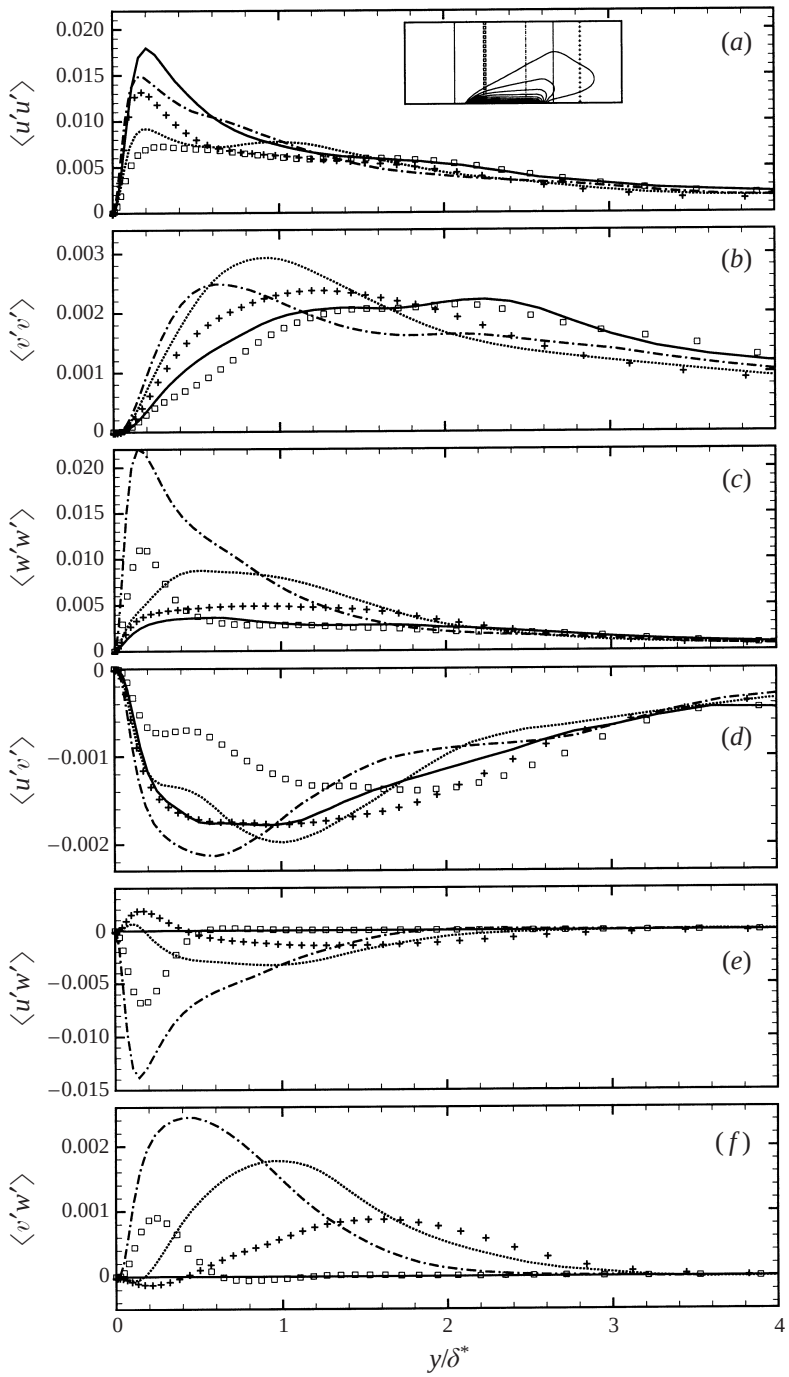

FIGURE 16. Profiles of the Reynolds stresses. ———, $x/\delta_r^* = 62$; □, $x/\delta_r^* = 98$; —·—, $x/\delta_r^* = 154$; ·····, $x/\delta_r^* = 185$; +, $x/\delta_r^* = 216$. (*a*) $\langle u'^2 \rangle$; (*b*) $\langle v'^2 \rangle$; (*c*) $\langle w'^2 \rangle$; (*d*) $\langle u'v' \rangle$; (*e*) $\langle u'w' \rangle$; (*f*) $\langle v'w' \rangle$.

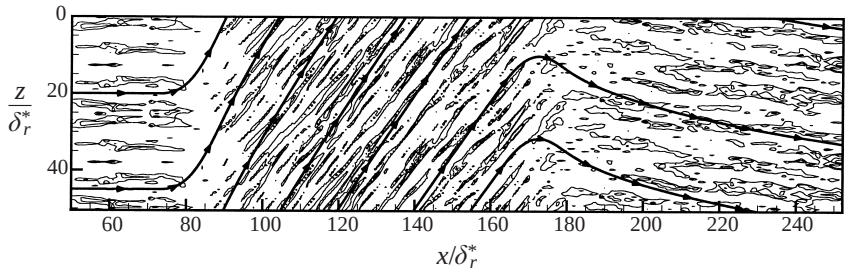

FIGURE 17. Contours of the negative streamwise velocity fluctuations in the $y/\delta_r^* = 0.15$ plane. The contour levels are -0.05, -0.1, -0.15, -0.2. The lines indicate the direction of the wall stress. Two domains are shown side by side.

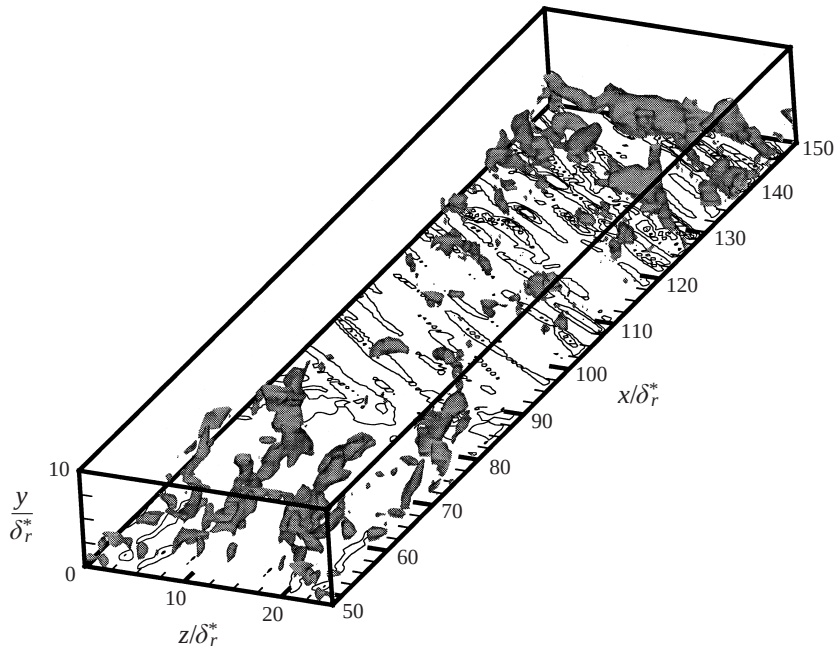

FIGURE 18. Low-pressure ($p = -0.004\rho U_\infty^2$) iso-surfaces superimposed on contours of the wall enstrophy (the contour levels are 10, 20 and $30U_\infty^2/\delta_r^{*2}$).

motion is applied, $\langle u'v' \rangle$ decreases significantly (figure 16*d*). Moin *et al.* (1990) and Coleman *et al.* (1996) also observed a similar decrease in their DNS of temporally developing three-dimensional channel flows; Moin *et al.* (1990) attributed it to changes in the pressure–strain correlation, whereas Sendstad & Moin (1992) and Coleman *et al.* (1996) related it to the structural features of the flow, namely the fact that the spanwise shear tears the streaks apart, thereby modifying their interaction with the near-wall vortical structures. The data by Coleman *et al.* (1996), in particular, show that the streaks first break down into shorter pieces, then align themselves with the direction of the wall stress, and finally coalesce to re-take their elongated shape. In the present calculation a similar behaviour is observed (figure 17).

Based on the results of their numerical experiments, Coleman *et al.* (1996) also conjectured that the shear imposed at the wall does not affect directly the near-wall

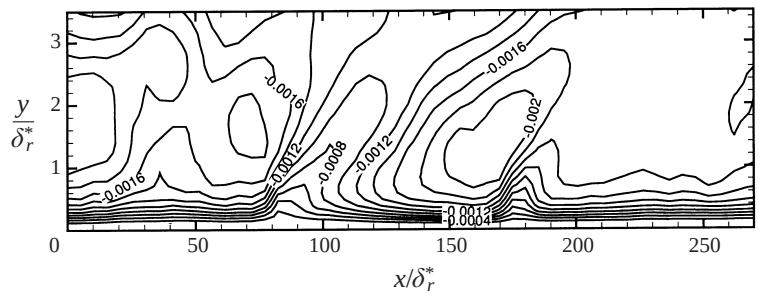

FIGURE 19. Contours of $\langle u'v' \rangle$, HSM case.

vortical structures, but only the streaks. The Reynolds stress is, therefore, reduced by the reduction of the interaction between streaks and vortical structures, rather than by a modification of the vortical structures *per se*. In the present study even the outer structures appear to be significantly modified. Figure 18 shows a visualization of the outer-layer vortical structures via low-pressure iso-surfaces, as well as contours of the enstrophy on the wall. In the two-dimensional region both quasi-streamwise vortices and arches can be observed. Following the imposition of the spanwise motion ($x/\delta_r^* \simeq 70$), the streaky structure of the viscous shear layer becomes less well-defined. The disturbance has to propagate a finite distance away from the wall, and by $x/\delta_r^* \simeq 90$ even the outer-layer vortical structure is affected, and significantly fewer structures are detected. Further downstream, new vortical structures are generated at the wall and convected towards the outer layer. The quasi-streamwise vortices are now oriented in the direction of the wall stress, at an angle of approximately 50° to the x-direction. Similar conclusions can be reached by examining enstrophy surfaces (not shown), which highlight the near-wall structures better than the pressure (which tends to isolate the outer eddies).

The propagation into the outer layer of the disturbance introduced at the wall can also be seen in the contours of the Reynolds shear stress $\langle u'v' \rangle$, shown in figure 19. The shear stress also begins decreasing shortly after the motion is imposed, and the perturbation reaches the outer flow at $x/\delta_r^* \simeq 90$.

The decrease of $\langle u'v' \rangle$ affects directly the production of $\langle u'^2 \rangle$, $\mathscr{P}_{11} \simeq -2\langle u'v' \rangle \partial U/\partial y$ (since $\partial U/\partial x \simeq 0$), which also decreases, as shown in figure 20. At the same time, the secondary stress $\langle v'w' \rangle$ appears (figure 16*f*). A significant mechanism for its generation is the production term $\mathscr{P}_{23} = -\langle u'v' \rangle \partial W/\partial x$, figure 21.

Due to the growth of the secondary Reynolds stress $\langle v'w' \rangle$, the production of $\langle w'^2 \rangle$, $\mathscr{P}_{33} \simeq -2\langle v'w' \rangle \partial W/\partial y$, becomes very large (figure 22), especially near the wall, where $\langle w'^2 \rangle$ begins to increase. At this streamwise position the production of $\langle w'^2 \rangle$ is larger than that of $\langle u'^2 \rangle$, and the peak $\langle w'^2 \rangle$ is three times its equilibrium two-dimensional value (figure 16*c*). In the near-wall region $\langle w'^2 \rangle > \langle u'^2 \rangle > \langle v'^2 \rangle$, while away from the wall, where the fluid has not yet been disturbed, $\langle u'^2 \rangle > \langle w'^2 \rangle > \langle v'^2 \rangle$, as in the two-dimensional case.

The wall-normal Reynolds stress $\langle v'^2 \rangle$ is not as strongly affected throughout the flow: as the perturbation is imposed, a small reduction of $\langle v'^2 \rangle$ can be observed. Its level, however, is generally increased towards the end of the plate as the flow approaches a collateral equilibrium state at a higher Reynolds number.

The budgets of $\langle u'^2 \rangle$ and $\langle w'^2 \rangle$ (figures 20 and 22) indicate that the velocity–pressure-gradient term plays a minor role in this exchange of energy between components, which is mainly driven by changes in the production. This confirms a conjecture by

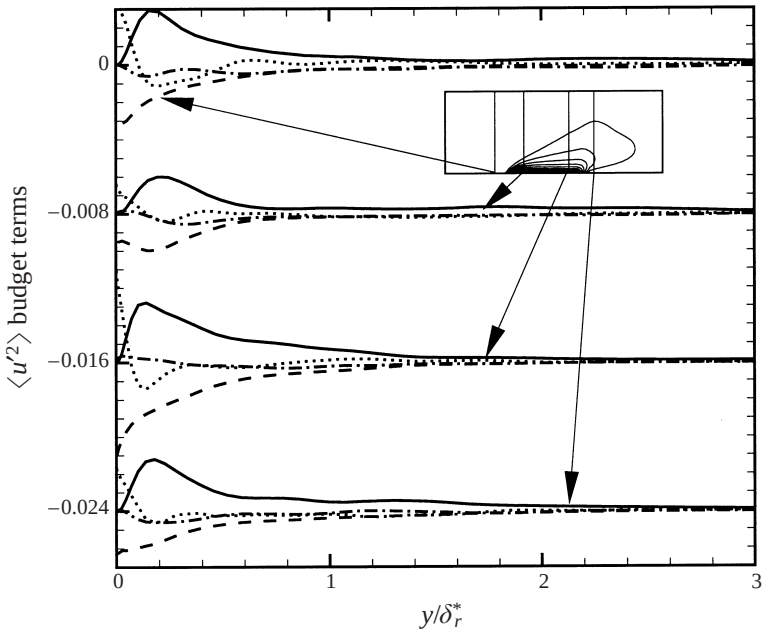

FIGURE 20. $\langle u'^2 \rangle$ Reynolds-stress budgets normalized by U_∞ and δ^*. ———, production; – – – –, dissipation; ·····, diffusion; —·—, velocity–pressure-gradient. From top to bottom, $x/\delta_r^* = 62$, 98, 154 and 185. Each set of curves is shifted downwards by 0.08 units for clarity.

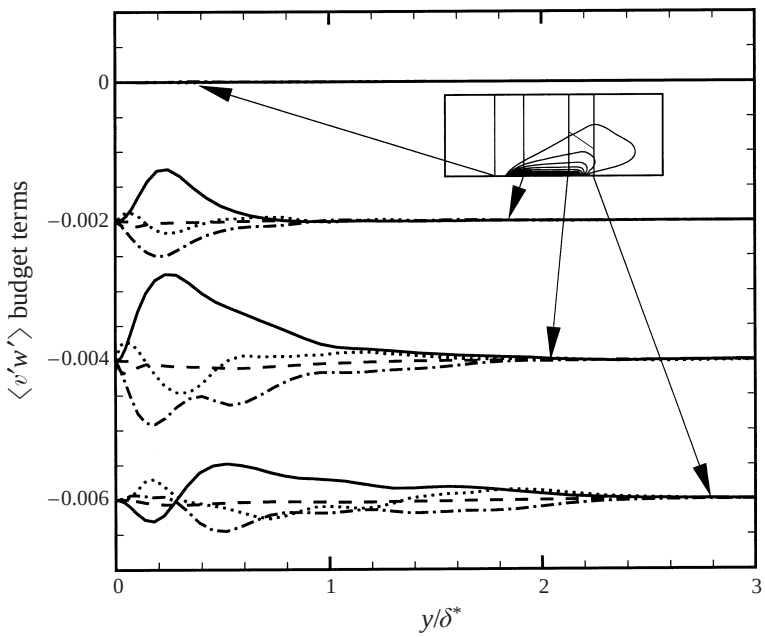

FIGURE 21. $\langle v'w' \rangle$ Reynolds-stress budgets normalized by U_∞ and δ^*. ———, production; – – – –, dissipation; ·····, diffusion; —·—, velocity–pressure-gradient. From top to bottom, $x/\delta_r^* = 62$, 98, 154 and 185. Each set of curves is shifted downwards by 0.02 units for clarity.

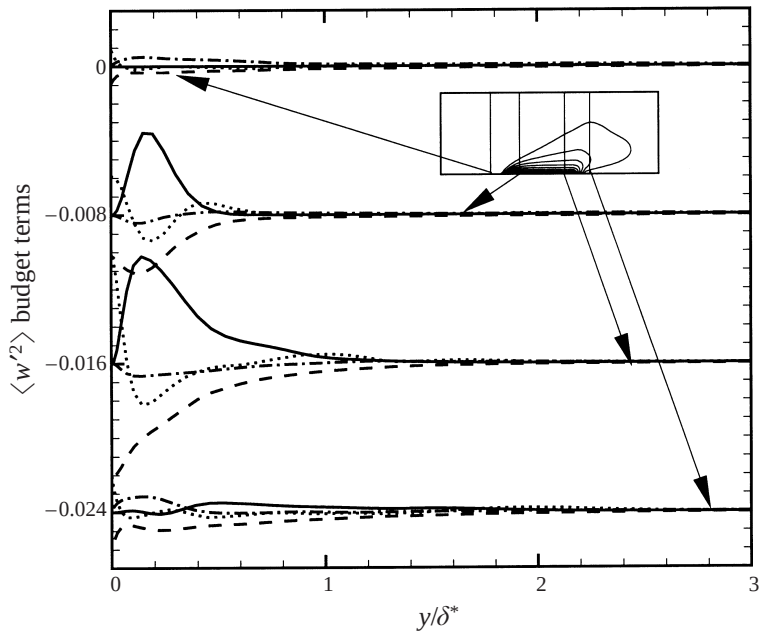

FIGURE 22. $\langle w'^2 \rangle$ Reynolds-stress budgets normalized by U_∞ and δ^*. ———, production; – – – –, dissipation; ·····, diffusion; —·—, velocity–pressure-gradient. From top to bottom, $x/\delta_r^* = 62$, 98, 154 and 185. Each set of curves is shifted downwards by 0.08 units for clarity.

Durbin (1993). A significant decrease of the magnitude of the dissipation of $\langle u'^2 \rangle$ is observed near the wall (consistent with the findings of Coleman *et al.* 1996); as a consequence, the diffusion at the wall decreases. Furthermore, to balance the decrease in production, the diffusion (which in the two-dimensional boundary layer changes sign twice) remains positive or near zero throughout the boundary layer.

Proceeding further along the plate, the streaks re-form (figure 17) and become elongated again. Due to the increased turbulence Reynolds number, they also appear thinner in outer coordinates. The fact that they are aligned in the direction of the wall stress, forming an angle of approximately 50° with the streamwise direction, is the reason for the very severe grid resolution requirements encountered in the present simulation, which had to be significantly refined in the streamwise direction in order to resolve the streaks over the moving surface.

Towards the trailing edge of the plate, in the quasi-collateral region, $\langle u'^2 \rangle$ has nearly regained its two-dimensional value, although it remains smaller than $\langle w'^2 \rangle$. The budgets of $\langle u'^2 \rangle$ and $\langle w'^2 \rangle$ recover shapes similar to those observed in the equilibrium, two-dimensional, boundary layer, although at much higher amplitudes. However, normalization by either the local Q_τ or its streamwise component, $u_{\tau,x}$, fails to collapse the data on the equilibrium curves. The fact that the length of the plate was insufficient to achieve a fully collateral condition may play a role in this.

On the moving plate $\langle v'w' \rangle$ continues to increase, due to increased production, and eventually becomes comparable to $\langle u'v' \rangle$. As often observed in three-dimensional flows, the secondary shear $\langle u'w' \rangle$ becomes larger than either $\langle u'v' \rangle$ or $\langle v'w' \rangle$. This term, however, does not contribute significantly to the production of any of the Reynolds stresses, except perhaps very near the trailing edge, where $\partial W/\partial x$ is significant (and

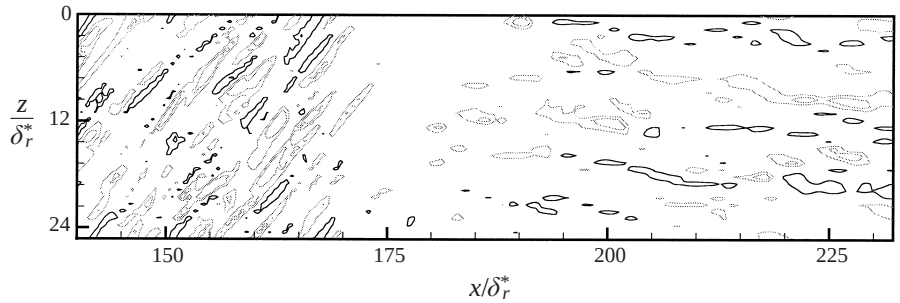

FIGURE 23. Contours of the streamwise velocity fluctuations in the $y/\delta_r^* = 0.15$ plane near the moving-plate trailing edge. The contour levels are ± 0.1 and ± 0.2. Negative contours are grey, positive are black.

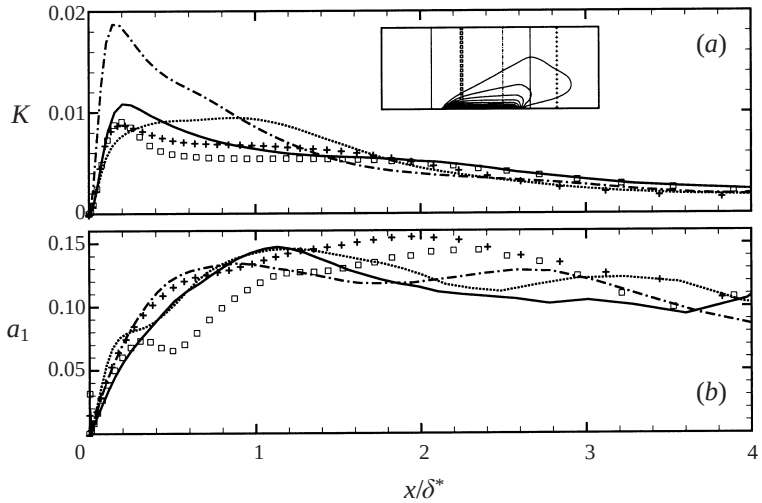

FIGURE 24. Profiles of the turbulent kinetic energy and structure parameter. ———, $x/\delta_r^* = 62$; □, $x/\delta_r^* = 98$; —·—, $x/\delta_r^* = 154$; ·····, $x/\delta_r^* = 185$; +, $x/\delta_r^* = 216$. (*a*) K; (*b*) a_1.

negative) and $\partial W/\partial y$ becomes positive, leading to a region of negative production of $\langle w'^2 \rangle$ near the wall.

Behind the trailing edge, phenomena similar to those observed at the leading edge occur: the streaks break up (figures 17 and 23) and form again, aligned with the wall stress (now returning towards the streamwise direction). As a consequence, $\langle u'v' \rangle$ decreases slightly, as does the production of $\langle u'^2 \rangle$. The production of $\langle w'^2 \rangle$ becomes negative, so that dissipation is balanced by the velocity–pressure-gradient term, and the spanwise Reynolds stress decays rapidly. The production of $\langle v'w' \rangle$ also becomes negative near the wall, since the spanwise flow decelerates strongly ($\partial W/\partial x < 0$). This results in a very rapid decay of $\langle v'w' \rangle$, which also changes sign in the near-wall region due to the negative $\mathscr{P}_{23}$.

Profiles of the turbulent kinetic energy and of the structure parameter a_1 are shown in figure 24. Despite the growth of $\langle w'^2 \rangle$, immediately after the leading edge of the plate K decreases from its two-dimensional value, consistent with the findings of Moin *et al.* (1990) and Coleman *et al.* (1996). The present calculation extended into the quasi-collateral region, in which K grows again and becomes larger than

in the equilibrium case; it decreases again after the trailing edge to return to its two-dimensional equilibrium value.

The structure parameter a_1 decreases near the wall immediately after the plate motion is started. The lower value of a_1 indicates that the boundary layer is less efficient in extracting shear stress from a given amount of turbulent kinetic energy. The reciprocal point of view can also be argued: perturbed boundary layers, which have additional production terms, are more efficient at generating turbulent kinetic energy from a given shear stress. This result is consistent, both quantitatively and qualitatively, with that of Coleman *et al.* (1996) in the shear-driven channel calculations, and with the high-spanwise-pressure-gradient case calculated by Moin *et al.* (1990) (in their baseline case the three-dimensional effects on a_1 were not as pronounced). These studies, however, concentrated on the initial stages of the response of the flow to the perturbation, and did not observe the return to the equilibrium value that we measured in the quasi-collateral region. A similar decrease is observed after the wall motion is ended, in the recovery region behind the moving plate.

The reduction of a_1 has been observed in several three-dimensional flows, both pressure driven (for instance, Bradshaw & Pontikos 1985; Anderson & Eaton 1989) and shear driven (Coleman *et al.* 1996). Since the net shear stress and the turbulent kinetic energy are invariant with respect to coordinate rotation in a plane parallel to the wall, Sendstad & Moin (1992) argued that this reduction in a_1 is not due to the rotation of the stress tensor or the strain vector, but to structural changes of turbulence due to three-dimensionality. Eaton (1992) explained it as the result of changes in the flow structure near the wall, which was hypothesized to be due to the crossflow decreasing the number of low-speed streaks and stress-producing burst–sweep mechanisms, as also claimed by Sendstad & Moin (1992). We also observe a decrease of the streak strength, as shown above. a_1, however, is also reduced in cases in which an equilibrium flow is subjected to a sudden perturbation, such as a flat-plate boundary layer subjected to an adverse (Spalart & Watmuff 1993) or to a favourable pressure gradient (Piomelli, Balaras & Pascarelli 2000). The decrease in a_1 may have two causes: inherent three-dimensionality in the flow (such as in the equilibrium Ekman layer calculated by Wu & Squires 1997), and non-equilibrium effects. In our calculations the reduction of a_1 appears to be associated with the response of the turbulence to the perturbation, rather than to three-dimensional effects *per se*, as indicated by the fact that, in the three-dimensional equilibrium region, a_1 recovers its two-dimensional value.

The budget of K is shown in figure 25. The significant decrease of the production term $-2\langle u'v'\rangle \partial U/\partial y$ that follows the beginning of the motion of the plate is not initially accompanied by a corresponding increase of $-2\langle v'w'\rangle \partial W/\partial y$; initially ($x/\delta_r^* < 90$), therefore the production of K decreases. As the secondary stress $\langle v'w'\rangle$ builds up, however, the production of K increases and by $x/\delta_r^* \simeq 98$ it is larger than in the two-dimensional boundary layer. The dissipation also decreases in that region, the decrease being more significant very near the wall, less so in the buffer region. The diffusion term, which in the two-dimensional boundary layer changes sign twice, in this region remains positive through the buffer and outer regions, to make up for the production deficit. After the initial region in which the production decreases, and the dissipation increases away from the wall but decreases in the inner layer, all the terms in the turbulent kinetic energy budget increase on the moving plate; their shape, however, is more similar to that of equilibrium two-dimensional boundary layers, reflecting the approach of collaterality on the plate.

As mentioned in the Introduction, Durbin (1993) proposed a Reynolds stress

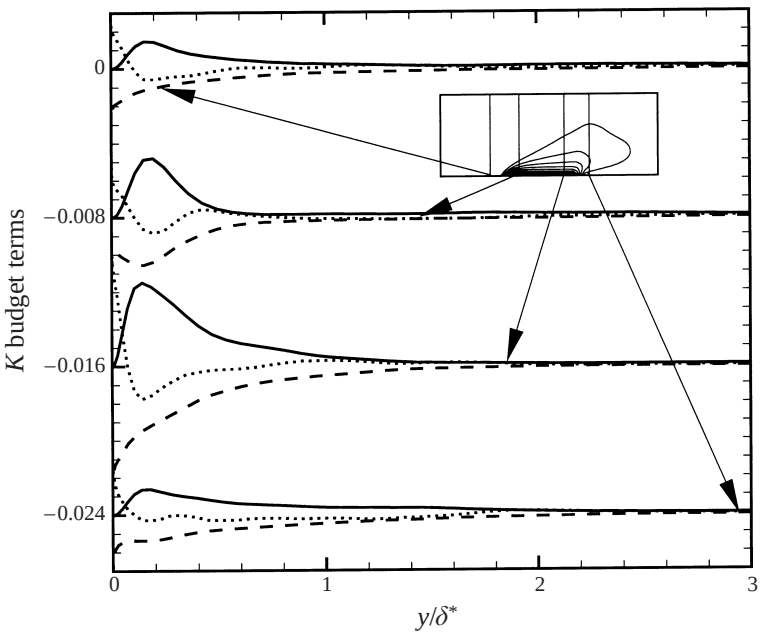

FIGURE 25. Turbulent kinetic energy budgets normalized by U_∞ and δ_r^*. ———, production; – – – –, dissipation; ·····, total diffusion (turbulent, SGS, pressure and viscous). From top to bottom, $x/\delta_r^* = 62$, 98, 154 and 185. Each set of curves is shifted downwards by 0.08 units for clarity.

model in which the ϵ-equation was modified to take into account the increase in the rate of energy dissipation observed, for instance, by Moin *et al.* (1990) in 3DTBLs. The increase of ϵ around $y^+ \simeq 10$ observed by Moin *et al.* (1990), was, however, accompanied by a reduction of ϵ close to the wall. We observe a similar trend: the dissipation at the wall decreases but it takes some time for the decrease to spread into the outer layers. There is a local maximum for the ϵ at a $y^+ \sim 10$ and a local minimum around $y^+ \simeq 5$ similar to Moin *et al.* (1990). The turbulent kinetic energy dissipation obtained from the present calculation follows similar trends. However, significant modifications in the diffusion and transport terms are also observed.

The Reynolds-stress distribution on the moving plate and in the recovery region is quite complex, and is governed by a combination of competing mechanisms. It should not be surprising, therefore, that simple eddy-viscosity-type turbulence models for the Reynolds-averaged Navier–Stokes (RANS) equations have not been successful in modelling flows of this type. As an illustration of the difficulties that this type of models encounters, in figure 26(*a*) the difference between the mean flow strain-rate angle, γ_g, and the Reynolds shear-stress angle, γ_τ, is shown. The two angles are defined as

$$\gamma_g = \tan^{-1}\frac{\partial W/\partial y}{\partial U/\partial y}, \quad \gamma_\tau = \tan^{-1}\frac{\langle v'w'\rangle}{\langle u'v'\rangle}. \tag{3.9}$$

In an equilibrium boundary layer, these two angles are equal. Immediately after the leading and trailing edges of the moving section, the Reynolds-shear-stress vector points in a different direction than the strain-rate vector, especially near the wall. As the flow returns towards a three-dimensional or two-dimensional equilibrium, this difference is reduced. The shear-stress vector always lags the strain-rate vector. Far away from the wall, these vectors become aligned and point in the mean flow direction.

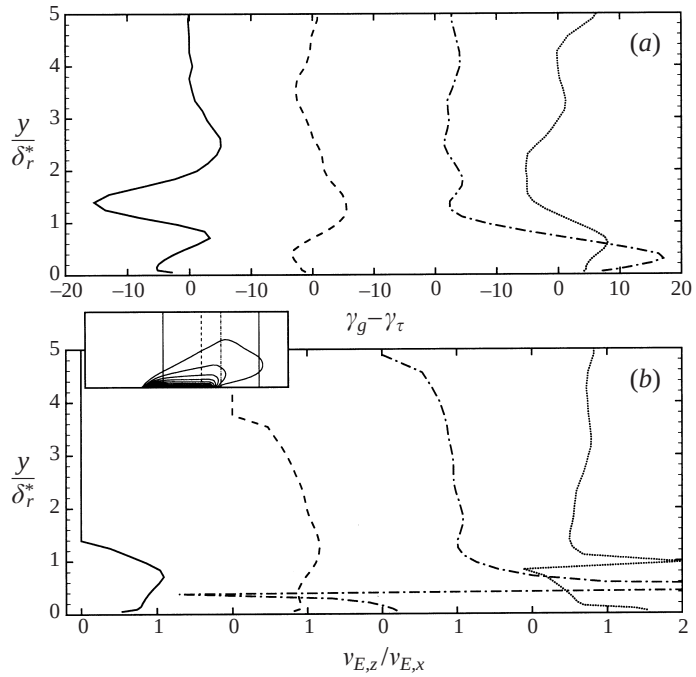

FIGURE 26. Profiles of flow angles and ratio of RANS eddy viscosities. ———, $x/\delta_r^* = 103$, – – –, $x/\delta_r^* = 154$, —·—, $x/\delta_r^* = 180$, ·····, $x/\delta_r^* = 230$. $W_s/U_\infty = 1.0$, HSM case. (*a*) $\gamma_g - \gamma_\tau$; (*b*) eddy viscosity ratio.

Eddy-viscosity models, furthermore, assume an isotropic eddy viscosity. Figure 26(*b*) shows the ratio of the spanwise and streamwise components of the eddy viscosity, defined as

$$\nu_{E,x} = -\frac{\langle u'v' \rangle}{\partial U/\partial y}, \quad \nu_{E,z} = -\frac{\langle v'w' \rangle}{\partial W/\partial y}. \tag{3.10}$$

The eddy viscosity is strongly anisotropic in the non-equilibrium regions. This behaviour is particularly marked in the recovery region, in which $\partial W/\partial y$ goes through zero (resulting in the discontinuities observed in the figure for the third and fourth profiles). This behaviour is very difficult to predict using RANS-type models. Ölçmen & Simpson (1995) report a similar behaviour for their pressure-driven boundary layer and show a discontinuity in their eddy-viscosity profiles.

4. Summary and conclusions

A shear-driven spatially developing three-dimensional turbulent boundary layer was studied by large-eddy simulation. The results compare fairly well with the available experimental data. This was the first investigation of spatially developing flows in which the near-wall structure of the flow could be studied, since previous experimental work was limited to outer-layer measurements, and numerical simulations were performed in temporally developing flows. Furthermore, both the response of the turbulence to the perturbation and its return to equilibrium are investigated.

The mean flow behaviour is found to be drastically changed when compared to the two-dimensional case. Most flow turning is observed within $y/\delta^* \approx 1$. The mean spanwise velocity profiles are self-similar when non-dimensionalized with respect to

the wall velocity, W_s: W behaves like an independent Stokes layer; in fact the growth rate of the transverse boundary layer, $\delta_z^* \sim x^{1/2}$ is similar to that of the laminar Stokes layer, $\delta \sim t^{1/2}$. Except very near the wall, an equilibrium is established between advection and the sum of turbulent and viscous diffusion.

On the moving wall a collateral condition of the flow is approached. The kinematic condition of collaterality forces the ratio of $c_{f,x}$ and $c_{f,z}$, and hence the surface-flow angle, to remain constant. There is a large drop in the wall shear stress in the axial direction, while the secondary wall shear stress in the spanwise direction increases. The spanwise skin friction also exhibits self-similarity, for the wall velocities examined, when normalized by $U_\infty W_s$.

In the near-wall region the flow accelerates strongly on the moving plate, and mildly downstream of it. This flow acceleration causes velocity deficits in the upper regions that slowly move upwards downstream, similar to the experimental findings of Lohmann (1976). On the moving wall, the law of the wall is observed to hold when expressed in terms of the resultant velocity relative to the moving plate and the resultant skin friction. However, the slope of the logarithmic layer decreases with increasing wall-to-free-stream speed ratio.

The flow structures are also drastically changed in the presence of three-dimensionality. The streaky structures in the viscous wall layer are torn by the imposed wall shear, causing an immediate reduction of the Reynolds shear stress $\langle u'v' \rangle$. Similar observations were made by Sendstad & Moin (1992) for pressure-driven channel flow, and by Coleman *et al.* (1996) for temporally developing channel flow. In addition, we observed that the outer-layer vortical structures are also disrupted, some distance downstream of the plate beginning, as the disturbance propagates away from the wall. On the moving plate new, more energetic, structures are generated, which align themselves with the direction of the wall shear. Behind the trailing edge of the moving plate similar phenomena take place.

Following the drop in $\langle u'v' \rangle$, $\langle u'^2 \rangle$ and K also decrease close to the junctions of the moving plate. As new eddies are formed in the direction of the wall shear the secondary Reynolds stress $\langle v'w' \rangle$ increases, supplying an additional production term for $\langle w'^2 \rangle$, which becomes larger than $\langle u'^2 \rangle$. The turbulent kinetic energy also increases above its two-dimensional equilibrium value. The structure parameter a_1 decreases below its two-dimensional value following the imposition of the wall motion, but then recovers its equilibrium value. This indicates that the reduction of the structure parameter may be due more to the effects of the perturbation away from equilibrium than to three-dimensional effects *per se*. Another decrease of $\langle u'v' \rangle$, a_1 and K follows the trailing edge of the moving plate, followed by recovery of the two-dimensional values.

The changes in the normal Reynolds stresses and turbulent kinetic energy are mostly due to changes in the production; the dissipation responds more slowly to the imposition of the perturbation, except very near the wall. The pressure only plays a minor role. In the budgets of K and $\langle u'^2 \rangle$, the diffusion term changes sign under non-equilibrium conditions in order to account for the different adjustment times of production and dissipation. For the shear stresses $\langle u'v' \rangle$ and $\langle v'w' \rangle$, production is balanced by the velocity–pressure gradient for $y^+ < 15$. Although the dissipation of $\langle u'v' \rangle$ and $\langle v'w' \rangle$ can be neglected, the dissipation of $\langle u'w' \rangle$ is significant and non-negligible. This implies that an isotropic assumption for the dissipation tensor is violated in such flows.

The stress angle is found to be lagging the strain angle, as in the experiments. Near the wall there is considerable difference between the two, confirming the known anisotropy of the eddy viscosity: $\nu_{E,x} \neq \nu_{E,z}$.

This work was sponsored by the Office of Naval research under Grant No. N00014-91-J-1638, monitored by Drs L. Patrick Purtell and Candace Wark. Computer time was supplied by CEWES/NAVO.

REFERENCES

Anderson, S. D. & Eaton, J. K. 1989 Reynolds stress development in pressure-driven, three-dimensional, turbulent boundary layers. *J Fluid Mech.* **202**, 263–294.

Antonia, R. A. & Luxton, R. E. 1971 The response of a turbulent boundary layer to an upstanding step change in surface roughness. *Trans. ASME* D: *J. Basic Engng* **93**, 22–34.

Bissonnette, L. R. & Mellor, G. L. 1974 Experiments on the behaviour of an axisymmetric turbulent boundary layer with a sudden circumferential strain. *J. Fluid Mech.* **63**, 369–413.

Bradshaw, P. 1987 Turbulent secondary flows. *Ann. Rev. Fluid Mech.* **19**, 53–74.

Bradshaw, P., Launder, B. E. & Lumley, J. L. 1996 Collaborative testing of turbulence models. *Trans. ASME* I: *J. Fluids Engng* **118**, 243–247.

Bradshaw, P. & Pontikos, N. S. 1985 Measurements in the turbulent boundary layer on an 'infinite' swept wing. *J. Fluid Mech.* **159**, 105–130.

Chorin, A. J. 1967 Numerical solution of the Navier–Stokes equations. *Math. Comput.* **22**, 745–762.

Clauser, F. 1954 Turbulent boundary layers in adverse pressure gradients. *J. Aero. Sci.* **21**, 91–108.

Coleman, G. N., Kim, J. & Le, A. T. 1996 A numerical study of three-dimensional wall-bounded flows. *Intl J. Heat Fluid Flow* **17**, 333–342.

Cousteix, J. 1986 Three-dimensional and unsteady boundary layer computations. *Ann. Rev. Fluid Mech.* **18**, 173–196.

Driver, D. M. & Hebbar, S. K. 1987 Experimental study of a three-dimensional, shear-driven, turbulent boundary layer. *AIAA J.* **25**, 35–42.

Driver, D. M. & Johnston, J. P. 1990 Experimental study of a three-dimensional shear-driven turbulent boundary layer with streamwise adverse pressure gradient. *NASA TM* 102211.

Durbin, P. A. 1993 On modeling three-dimensional turbulent wall layers. *Phys. Fluids* A **5**, 1231–1238.

Eaton, J. K. 1992 Turbulence structure and heat transfer in three-dimensional boundary layers. In *Proc. 6th Symp. Energy Engineering Sciences, CONF–9105116*, p. 262. DOE Publications.

Fannelop, T. K. & Krogstad, P. A. 1975 Three-dimensional turbulent boundary layers in external flows: a report on Euromech 60. *J. Fluid Mech.* **71**, 815–826.

Fernholz, H. H. & Vagt, J. D. 1981 Turbulence measurements in an adverse pressure gradient three-dimensional turbulent boundary layer along a circular cylinder. *J. Fluid Mech.* **111**, 233–269.

Germano, M., Piomelli, U., Moin, P. & Cabot, W. H. 1991 A dynamic subgrid-scale eddy viscosity model. *Phys. Fluids* A **3**, 1760–1765.

Higuchi, H. & Rubesin, M. W. 1979 Behavior of a turbulent boundary layer subjected to sudden transverse strain. *AIAA J.* **17**, 931–941.

Huai, X., Joslin, R. D. & Piomelli, U. 1997 Large-eddy simulation of transition to turbulence in boundary layers. *Theor. Comput. Fluid Dyn.* **9**, 149–163.

Huai, X., Joslin, R. D. & Piomelli, U. 1999 Large-eddy simulation of boundary-layer transition on a swept wedge. *J. Fluid Mech.* **381**, 357–380.

Johnston, J. P. 1960 On the three-dimensional turbulent boundary layer generated by secondary flow. *Trans. ASME* D: *J. Basic Engng* **82**, 233–248.

Johnston, J. P. 1970 On the three-dimensional turbulent boundary layer induced by a swept, forward-facing step. *J. Fluid Mech.* **42**, 823–844.

Johnston, J. P. & Flack, K. A. 1996 Review – Advances in three-dimensional turbulent boundary layers with emphasis on the wall-layer regions. *Trans. ASME* I: *J. Fluids Engng* **118**, 219–232.

Joslin, R. D., Streett, C. L. & Chang, C.-L. 1993 Spatial direct numerical simulation of boundary-layer transition mechanisms: Validation of PSE theory. *Theor. Comput. Fluid Dyn.* **4**, 271–288.

Lilly, D. K. 1992 A proposed modification of the Germano subgrid-scale closure method. *Phys. Fluids* A **4**, 633–635.

Liu, J., Piomelli, U. & Spalart, P. R. 1996 Interaction between a spatially growing turbulent boundary layer and embedded streamwise vortices. *J. Fluid Mech.* **326**, 151–179.

LOHMANN, R. P. 1976 Response of a developed turbulent boundary layer to local transverse surface motion. *Trans. ASME* I: *J. Fluids Engng* **98**, 354–363.

MOIN, P., SHIH, T. H., DRIVER, D. & MANSOUR, N. N. 1990 Direct numerical simulation of a three-dimensional turbulent boundary layer. *Phys. Fluids* A **2**, 1846–1853.

NEVES, J. C., MOIN, P. & MOSER, R. D. 1994*a* Effects of convex transverse curvature on wall-bounded turbulence. Part 1. The velocity and vorticity. *J. Fluid Mech.* **272**, 349–381.

NEVES, J. C., MOIN, P. & MOSER, R. D. 1994*b* Effects of convex transverse curvature on wall-bounded turbulence. Part 2. The pressure fluctuations. *J. Fluid Mech.* **272**, 383–406.

ÖLÇMEN, M. S. & SIMPSON, R. L. 1993 Evaluation of algebraic eddy-viscosity models in three-dimensional turbulent boundary layers. *AIAA J.* **31**, 1545–1554.

PARNEIX, S. & DURBIN, P. A. 1997 Numerical simulation of 3D turbulent boundary layers using the V2F model. In *Center for Turbulence Research Annual Research Briefs 1997*, pp. 135–148. Stanford University.

PIERCE, F. J. & MCALLISTER, J. E. 1983*a* A review of near-wall similarity models in three-dimensional turbulent boundary layers. *Trans. ASME* I: *J. Fluids Engng* **105**, 251–256.

PIERCE, F. J. & MCALLISTER, J. E. 1983*b* Near-wall similarity in a pressure-driven three-dimensional turbulent boundary layer. *Trans. ASME* I: *J. Fluids Engng* **105**, 257–262.

PIERCE, F. J. & MCALLISTER, J. E. 1983*c* Near-wall similarity in a shear-driven three-dimensional turbulent boundary layer. *Trans. ASME* I: *J. Fluids Engng* **105**, 263–269.

PIOMELLI, U., BALARAS, E. & PASCARELLI, A. 2000 Turbulent structures in accelerating boundary layers. *J. Turbulence* **1**, 1–16. ISSN: 1468-5248.

PIOMELLI, U. & LIU, J. 1995 Large-eddy simulation of rotating channel flows using a localized dynamic model. *Phys. Fluids* **7**, 839–848.

ROTTA, J. C. 1979 A family of turbulence models for three-dimensional boundary layers. In *Turbulent Shear Flows I* (ed. F. Durst, B. E. Launder, F. W. Schmidt & J. H. Whitelaw), pp. 267–278. Springer.

SENDSTAD, O. & MOIN, P. 1992 The near wall mechanics of three-dimensional turbulent boundary layers. *Rep.* TF-57. Thermosciences Division, Department of Mechanical Engineering, Stanford University.

SPALART, P. R. 1988 Direct numerical simulation of a turbulent boundary layer upto $Re_\theta = 1410$. *J. Fluid Mech.* **187**, 61–98.

SPALART, P. R. & WATMUFF, J. H. 1993 Experimental and numerical study of a turbulent boundary layer with pressure gradients. *J. Fluid Mech.* **249**, 337–371.

SPEZIALE, C. G. 1991 Analytical methods for the development of Reynolds-stress closures in turbulence. *Ann. Rev. Fluid Mech.* **23**, 107–157.

STREETT, C. L. & MACARAEG, M. G. 1989 Spectral multi-domain technique for large-scale fluid-dynamic simulations. *Appl. Numer. Maths* **6**, 123–139.

WHITE, F. M. 1991 *Viscous Fluid Flow*, 2nd Edn. McGraw-Hill.

WU, X. & SQUIRES, K. D. 1997 Large eddy simulation of an equilibrium three-dimensional turbulent boundary layer. *AIAA J.* **35**, 67–74.

WU, X. & SQUIRES, K. D. 1998 Prediction of the three-dimensional turbulent boundary layer over a swept bump. *AIAA J.* **36**, 505–514.

ZANG, Y., STREET, R. L. & KOSEFF, J. 1993 A dynamic mixed subgrid-scale model and its application to turbulent recirculating flows. *Phys. Fluids* A **5**, 3186–3196.